Remote Sensing of Environment 210 (2018) 113–143

Contents lists available at ScienceDirect

Remote Sensing of Environment

journal homepage: www.elsevier.com/locate/rse

NASA's Black Marble nighttime lights product suite

Miguel O. Román[a,*], Zhuosen Wang[b,a], Qingsong Sun[c,a], Virginia Kalb[a], Steven D. Miller[d], Andrew Molthan[f,e], Lori Schultz[e,f], Jordan Bell[e,f], Eleanor C. Stokes[g], Bhartendu Pandey[g], Karen C. Seto[g], Dorothy Hall[b], Tomohiro Oda[h,i], Robert E. Wolfe[a], Gary Lin[j,a], Navid Golpayegani[a], Sadashiva Devadiga[j,a], Carol Davidson[j,a], Sudipta Sarkar[j,a], Cid Praderas[j,a], Jeffrey Schmaltz[j,a], Ryan Boller[k], Joshua Stevens[j,l], Olga M. Ramos González[m], Elizabeth Padilla[n], José Alonso[o], Yasmín Detrés[p], Roy Armstrong[p], Ismael Miranda[q], Yasmín Conte[r], Nitza Marrero[s], Kytt MacManus[t], Thomas Esch[u], Edward J. Masuoka[a]

[a] Terrestrial Information Systems Laboratory, NASA Goddard Space Flight Center, Greenbelt, MD, USA
[b] Earth System Science Interdisciplinary Center, University of Maryland College Park, College Park, MD, USA
[c] School for the Environment, University of Massachusetts Boston, Boston, MA, USA
[d] Cooperative Institute for Research in the Atmosphere, Fort Collins, CO, USA
[e] Earth Science Office, NASA Marshall Space Flight Center, Huntsville, AL, USA
[f] Earth System Science Center (ESSC), University of Alabama in Huntsville, Huntsville, AL, USA
[g] School of Forestry and Environmental Studies, Yale University, New Haven, CT, USA
[h] Global Modeling and Assimilation Office, NASA Goddard Space Flight Center, Greenbelt, MD, USA
[i] Goddard Earth Sciences Technologies and Research, Universities Space Research Association, Columbia, MD, USA
[j] Science Systems and Applications, Inc., Lanham, MD, USA
[k] Science Data Systems Branch, NASA Goddard Space Flight Center, Greenbelt, MD, USA
[l] NASA Earth Observatory, NASA Goddard Space Flight Center, Greenbelt, MD, USA
[m] GIS and Remote Sensing Laboratory, USDA Forest Service, International Institute of Tropical Forestry, Río Piedras, Puerto Rico
[n] Para La Naturaleza, San Juan, Puerto Rico
[o] Department of Mathematics-Physics, University Puerto Rico-Cayey Campus, Cayey, Puerto Rico
[p] Department of Marine Sciences, University of Puerto Rico Mayagüez Campus, Mayagüez, Puerto Rico
[q] Puerto Rico's Working Group on Light Pollution, San Juan, Puerto Rico
[r] University of Puerto Rico, Río Piedras Campus, San Juan, Puerto Rico
[s] Light Pollution Control Program, Environmental Quality Board, San Juan, Puerto Rico
[t] Center for International Earth Science Information Network (CIESIN), The Earth Institute, Columbia University, Palisades, NY, USA
[u] German Remote Sensing Data Center, German Aerospace Center (DLR), Oberpfaffenhofen, Germany

ARTICLE INFO

Keywords:
Suomi-NPP
JPSS
NASA black marble
VIIRS
Night lights
NTL
Urban dynamics
Long-term monitoring
Lunar BRDF
Albedo
Atmospheric correction

ABSTRACT

NASA's Black Marble nighttime lights product suite (VNP46) is available at 500 m resolution since January 2012 with data from the Visible Infrared Imaging Radiometer Suite (VIIRS) Day/Night Band (DNB) onboard the Suomi National Polar-orbiting Platform (SNPP). The retrieval algorithm, developed and implemented for routine global processing at NASA's Land Science Investigator-led Processing System (SIPS), utilizes all high-quality, cloud-free, atmospheric-, terrain-, vegetation-, snow-, lunar-, and stray light-corrected radiances to estimate daily nighttime lights (NTL) and other intrinsic surface optical properties. Key algorithm enhancements include: (1) lunar irradiance modeling to resolve non-linear changes in phase and libration; (2) vector radiative transfer and lunar bidirectional surface anisotropic reflectance modeling to correct for atmospheric and BRDF effects; (3) geometric-optical and canopy radiative transfer modeling to account for seasonal variations in NTL; and (4) temporal gap-filling to reduce persistent data gaps. Extensive benchmark tests at representative spatial and temporal scales were conducted on the VNP46 time series record to characterize the uncertainties stemming from upstream data sources. Initial validation results are presented together with example case studies illustrating the scientific utility of the products. This includes an evaluation of temporal patterns of NTL dynamics associated with urbanization, socioeconomic variability, cultural characteristics, and displaced populations affected by conflict. Current and planned activities under the Group on Earth Observations (GEO) Human Planet Initiative

* Corresponding author.
E-mail address: miguel.o.roman@nasa.gov (M.O. Román).

https://doi.org/10.1016/j.rse.2018.03.017
Received 4 November 2017; Received in revised form 7 March 2018; Accepted 11 March 2018
Available online 19 March 2018

are aimed at evaluating the products at different geographic locations and time periods representing the full range of retrieval conditions.

1. Introduction

The Day/Night Band (DNB) sensors of the Visible Infrared Imaging Radiometer Suite (VIIRS), on board the Suomi-National Polar-orbiting Partnership (S-NPP) and Joint Polar Satellite System (JPSS) satellite platforms, provide global daily measurements of nocturnal visible and near-infrared (NIR) light that are suitable for earth system science and applications studies. Since the launch of the S-NPP satellite in 2011, multiple studies have used the VIIRS DNB as primary data source covering a wide range of topics. These include: (1) feature extraction techniques, based on manual or semi-automated interpretation of the underlying VIIRS DNB radiances, to detect severe weather impacts to urban infrastructure (Cao et al., 2013; Cole et al., 2017; Mann et al., 2016; Molthan and Jedlovec, 2013); (2) detection of sub-pixel scale features, *e.g.*, fires (Polivka et al., 2016), shipping vessels (Asanuma et al., 2016; Elvidge et al., 2015; Straka et al., 2015), lightning flashes (Bankert et al., 2011), surface oil slicks (Hu et al., 2015), and gas flares (Elvidge et al., 2015; Liu et al., 2017, 2017); and (3) techniques for monitoring nighttime atmospheric optical properties, including clouds (Minnis et al., 2016; Walther et al., 2013), aerosols (Johnson et al., 2013; McHardy et al., 2015), particulate matter (Wang et al., 2016), and gravity waves in the upper atmosphere *via* nightglow (Miller et al., 2015).

As with early research that utilized the Defense Meteorological Satellite Program's Operational Line Scanner (DMSP/OLS) (Huang et al., 2014), recent studies using the VIIRS DNB have employed statistical analyses and correlation discovery methods to confirm established empirical relationships with a wide range of human-linked patterns and processes. These include socioeconomic variables (Chen and Nordhaus, 2015; Chen et al., 2015; Levin and Zhang, 2017; Li et al., 2013; Ma et al., 2014; Shi et al., 2014; Yu et al., 2015), as well as changes driven by urban built-up expansion (Guo et al., 2015; Sharma et al., 2016; Shi et al., 2014), energy use (Coscieme et al., 2014; Román and Stokes, 2015), and carbon emissions (Oda et al., 2017; Ou et al., 2015).

In order to make timely and quantitative use of nighttime lights (NTL), one must first quantify the subset of variations that are correlated to human-linked patterns and processes from those that are not. This requirement is especially true for products derived from the VIIRS DNB, given its ultra-sensitivity in low-lit conditions, and the resulting influence of extraneous light emission sources on the NTL time series record. Such artifacts can lead to discrepancies, *e.g.*, when using moon-free NTL composites as proxies to regional-scale socioeconomic features (Bickenbach et al., 2016; Chen and Nordhaus, 2015). To resolve retrieval uncertainties and measurement errors, the quality assurance of NTL products also needs to be emphasized, *e.g.*, by encouraging usage of quality flags that indicate the reliability of individual pixel values, or if retrievals are possibly affected by extraneous artifacts. More broadly, a meta-analysis of 132 research articles revealed the need to better trace the quality and provenance of NTL products as one of the most pressing areas of focus for future studies (Huang et al., 2014).

There is also a need to characterize uncertainties stemming from angular, diurnal, and seasonal variations in atmospheric and surface optical properties. This is crucial since, as we will present in this paper, NTL cannot be constrained directly from at-sensor top-of-atmosphere (TOA) radiances in part because of: (1) environmental factors, such as moon light, aerosols, and surface albedo whose reflectance contributes to the observed signal, and (2) errors stemming from seasonal variations and associated surface properties, which can significantly affect estimates of long-term trends. While it is generally neither desirable nor practical to delay the applied use of NTL products until they are proven to be error-free, or until known sources of error have been removed by product reprocessing, it is important to note that space agencies, coordinated by the Committee of Earth Observation Satellites (CEOS), place strong emphasis on product accuracy and performance. This information is needed by decision makers so they can trust the accuracy of the derived products, and by the science community, both to identify poorly performing products and opportunities for improvements, and to draw meaningful inferences from the long-term product records as they relate to trends in human settlements and urbanization.

There is increasing agreement in the growing body of literature concerning factors that govern the utilization of the VIIRS DNB for long-term analyses and applications. Recent studies have introduced a number of quantitative remote sensing techniques, including: (1) terrain-correction and trending of the VIIRS DNB geolocation (Wolfe et al., 2013); (2) establishing the calibration performance of the VIIRS DNB High Gain Stage (HGS), both in absolute terms and relative to future VIIRS flight units (Lee et al., 2015; Liao et al., 2013; Xiong et al., 2014; Zhang et al., 2016); (3) determining the effective spatial resolution and the impacts of spatial sampling on the VIIRS instrument and higher-level (Level 3) gridded products (Campagnolo et al., 2016; Pahlevan et al., 2017); (4) predicting the DNB's geometric characteristics (*i.e.*, time-varying Sun/Earth/Moon geometry, moon-illuminated fraction, phase, and albedo) (Miller et al., 2012a, 2012b); (5) estimating the highly variable TOA lunar spectral irradiance (Miller and Turner, 2009); (6) correcting for surface Bidirectional Reflectance Distribution Function (BRDF) effects caused by varying illumination conditions – namely moonlight and reflected airglow from the Earth's upper atmosphere (Cao et al., 2013; Cao and Bai, 2014; Román and Stokes, 2015; Zeng et al., 2018); and (7) assessing seasonal biases caused by sensor-specific stray light (Lee et al., 2015; Liao et al., 2013; Mills and Miller, 2016), as well as other biogeophysical processes, such as vegetation (Levin, 2017; Levin and Zhang, 2017) and snow cover (Bennett and Smith, 2017).

Despite this progress, substantial gaps remain in the quantification and documentation of uncertainty for NTL data and products. Such information is required by space agencies, such as the CEOS Working Group on Calibration and Validation (CEOS-WGCV). This development is particularly relevant if these products are to be used to establish global metrics and indicators for achieving a myriad of goals identified under the United Nations Agenda 2030 for Sustainable Development (Griggs et al., 2015). These sustainable development goals (SDGs) include: (1) addressing the needs of conflict-affected populations (SDG-1); (2) quantifying the effectiveness of local electrification projects in the developing world (SDG-7); (3) building resilient infrastructure, promote inclusive and sustainable industrialization and foster innovation (SDG-9); and (4) ensuring that cities and human settlements are inclusive, safe, resilient, and sustainable (SDG-11).

While the current Joint Polar Satellite System (JPSS) requirements establish performance metrics for the VIIRS DNB calibration and sensor characteristics, the current DNB-associated key performance requirements are tied strictly to nighttime imagery for short-term operational weather applications at high latitudes (Hillger et al., 2013). Whereas these formalized performance metrics correspond to the “Threshold” requirements of Table 1, the “Breakthrough” and “Goal” values point to 1–2 orders of magnitude improvement in sensitivity and spatial resolution. Here, “Threshold” is defined as the minimum requirement to be met to ensure that NTL time series data are useful, and is based on the current JPSS on-orbit performance requirements for the VIIRS DNB's High Gain Stage (HGS) calibration (Liao et al., 2013). The “Goal”

Table 1
Key performance metrics established for NASA's Black Marble product suite.

Key performance metrics	Threshold	Breakthrough	Goal
NTL detection limit (L_{min})	3.0 nW·cm^{-2}·sr^{-1}	0.5 nW·cm^{-2}·sr^{-1}	0.25 nW·cm^{-2}·sr^{-1}
NTL robustness (L_0)	± 3.0 nW·cm^{-2}·sr^{-1}	± 0.10 nW·cm^{-2}·sr^{-1}	± 0.05 nW·cm^{-2}·sr^{-1}
Stray light error	0.45 nW·cm^{-2}·sr^{-1}	0.25 nW·cm^{-2}·sr^{-1}	< 0.1 nW·cm^{-2}·sr^{-1}
Spatial resolution	742 m (± 5%)	500 m (± 5%)	≤200 m (± 5%)
Temporal resolution	Monthly	Daily	Hourly
Geolocation uncertainty	133 m	50 m	20 m

is an envisioned ideal requirement above which further improvements are not necessary to achieve all the science and applications underpinning global NTL data products. The "Breakthrough" is an intermediate level between "Threshold" and "Goal", which, if achieved, would result in a significant improvement (WMO, 2016). L_{min} is the minimum detectable NTL radiance and L_0 is the robustness or uncertainty (standard deviation) with respect to L_{min}. All values in Table 1 pertain to Land-based NTL detections.

To realize the full potential of the VIIRS DNB time series record for NTL applications, a new suite of standard products, hereby termed NASA's Black Marble product suite (VNP46) and representing the current state-of-the-art, was developed (Fig. 1). Key capabilities of the VNP46 products, described in subsequent sections, include:

(i) Daily frequency: The VNP46 product suite provides high-quality nightly NTL characterization based on cloud-free, atmospheric-, terrain-, vegetation-, snow-, lunar-, and stray light-corrected DNB radiances. This product enables first-ever detection of all nighttime light-related changes (*i.e.*, abrupt-, seasonal, and gradual changes – see examples in Figs. 15-16), at the native DNB pixel scale, in analysis-ready file formats (Level 3 gridded products).
(ii) Atmospheric correction: The VNP46 algorithm relies on the use of vector radiative transfer modeling of the coupled atmosphere-surface system (Vermote and Kotchenova, 2008) to compensate for aerosols, water vapor, and ozone impacts on the nighttime lights radiances (see Section 2.1). This correction mitigates errors stemming from poor-quality TOA retrievals, especially across regions with heavy aerosol loadings and at Moon/sensor geometries yielding stronger forward scatter contributions.
(iii) BRDF correction: The VNP46 algorithm estimates the actual moonlight, aerosol, and surface albedo contribution through analytical BRDF model inversion. This model has proven effective in removing biases introduced by extraneous sources of nighttime lights emissions (see Section 2.2).
(iv) Seasonal correction: Independent studies have demonstrated the need to correct for uncertainties stemming from seasonal variations in NTL time series data (Bennett and Smith, 2017; Bennie et al., 2014; Cinzano et al., 2000; Katz and Levin, 2016; Levin, 2017; Levin and Zhang, 2017). The VNP46 algorithm routinely accounts for these effects using well-established canopy radiative transfer methods applied using VIIRS data (see Section 2.3).

In this paper, we provide an overview of NASA's Black Marble research activities to-date. This includes a description of the algorithm and processing strategy (Section 2), details of the product suite based on six years of reprocessed data (Section 3–4), evaluation of its performance (Section 5), and example case studies illustrating the scientific utility and potential applications of the products (Section 6). The current (Collection V001) NASA Black Marble product suite, including daily at-sensor TOA nighttime radiances (VNP46A1) and daily moonlight adjusted NTL (VNP46A2), will begin operational processing in 2018. These data will be made available both retrospectively, *via* NASA's Level 1 and Atmosphere Archive and Distribution System (LAADS), and in forward (near-real time) data streams, *via* NASA's Land, Atmosphere Near Real-time Capability for EOS (LANCE).

2. Retrieval strategy

The operational NASA Black Marble product suite (VNP46) ingests multiple source datasets and ancillary data to output the highest quality pixel-based estimates of NTL. These NTL estimates are accompanied by pixel-level quality flags (see Appendix). The principal features of the algorithm are illustrated in Fig. 3, and are summarized in the following sections.

2.1. Atmospheric correction

NASA's Black Marble retrieval strategy combines daytime VIIRS DNB surface reflectance, Bidirectional Reflectance Distribution Function (BRDF), Surface Albedo, Nadir BRDF-Adjusted Reflectance

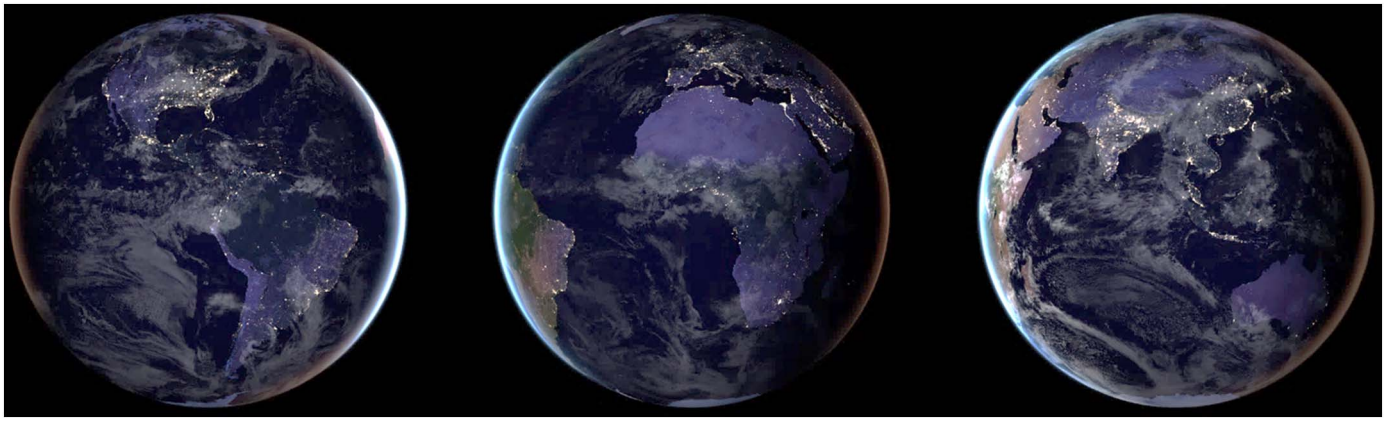

Fig. 1. NASA Black Marble composite images for year 2016 provide full-hemisphere views of Earth at night. Natural surfaces, clouds, and sun glint — added here for aesthetic effect — are derived from the MODIS Blue Marble Next Generation imagery products. (For interpretation of the references to colour in this figure legend, the reader is referred to the web version of this article.)

(NBAR), and Lunar irradiance values to minimize the biases caused by extraneous artifacts in the VIIRS NTL time series record.

Using this novel "turning off the Moon" approach, illustrated in Fig. 2, the surface upward radiance from artificial light emissions, L_{NTL} [units of nWatts·cm^{-2}·sr^{-1}], can be extracted from at-sensor nighttime radiances at TOA, L_{DNB}, using the following equation:

$$L_{NTL} = \left[\left(\frac{L_{DNB} - L_{path}}{T_{\uparrow}(\tau\theta_v)}\right)(1 - a(\theta_m)\rho_a) - L_m T_{\downarrow}(\tau\theta_v)\right]/P_{\uparrow}(\theta_v) \quad (1)$$

where L_{path} is the nighttime path radiance (*i.e.*, the radiance generated by scattering within the atmosphere), and $a(\theta_m)$ is the VIIRS-derived actual (or Blue-Sky) surface albedo; incorporating the directional influence of sky radiance and multiple scattering effects between the ground and the atmosphere (Román et al., 2010). For the latter, a snow albedo retrieval scheme is used if the VIIRS current day snow status flag is activated (Klein and Stroeve, 2002; Liu et al., 2017, 2017; Moustafa et al., 2017; Wang et al., 2012). $P_{\uparrow}(\theta_v)$ is defined in Eq. (10) (see Section 2.3 for details). The atmospheric backscatter is given by ρ_a, and $T_{\downarrow}(\tau,\theta_v)$ and $T_{\uparrow}(\tau,\theta_v)$ are the total transmittances (including direct and diffuse radiation) along the lunar-ground and ground-sensor paths (respectively). The latter two are a function of view-illumination geometry and the total atmospheric column optical depth (τ) due to mixed gases, water vapor, and aerosol particles. The retrieval uses a modified algorithm based on the heritage VIIRS Surface Reflectance product (VNP09) to estimate the values of L_{path}, ρ_a, $T_{\downarrow}(\tau,\theta_v)$, and $T_{\uparrow}(\tau,\theta_v)$ for a given set of surface and atmospheric conditions (Roger et al., 2016; Skakun et al., 2018). Additional input datasets include the standard VIIRS Cloud Mask (VCM) (Kopp et al., 2014), atmospheric profiles obtained from National Centers for Environmental Prediction (NCEP) model inputs (*i.e.*, water vapor, ozone, and surface pressure) (Moorthi et al., 2001), and the VIIRS aerosol model combined with daytime-to-daytime averaged Aerosol Optical Depth (AOD 0.550 μm) to extrapolate the nighttime AOD.

2.2. BRDF correction

The surface Bidirectional Reflectance Distribution Function (BRDF, or reflectance anisotropy) is governed by the angle and intensity of illumination – whether that illumination be solar or lunar or from airglow emissions – and by the structural complexity of the surface, resulting in variations in brightly illuminated regions and darkly shadowed areas. The semi-empirical RossThick-LiSparse Reciprocal (RTLSR, or Ross-Li) BRDF model (Román et al., 2010; Roujean et al., 1992; Schaaf et al., 2002, 2011; Strahler et al., 1999) is advantageous in this regard, since (1) it is the most likely kernel-driven combination to capture the wide range of conditions affecting the VIIRS DNB on a global basis; (2) it allows robust analytical model inversion with a pixel-specific estimate of uncertainty in the model parameters and linear combinations thereof (Lucht and Roujean, 2000); and (3) the scheme is flexible enough that other kernels can be easily adopted should any become available and should they be shown to be superior for a particular scenario.

For VIIRS DNB acquisitions over snow-free and snow-covered surfaces, we define the spectral radiance contribution from moonlight, L_m,

$$L_m(\Omega_v, \Omega_m, \Lambda) = \frac{E_m(\Lambda)}{\pi} BRF(\Omega_v, \Omega_m, \Lambda) cos(\theta_m) \quad (2)$$

in terms of the Ross-Li model:

$$BRDF(\Omega_v, \Omega_m, \Lambda) \approx \frac{BRF(\Omega_v, \Omega_m, \Lambda)}{\pi} = f_{iso}(\Lambda) + f_{vol}(\Lambda) K_{vol}(\Omega_v, \Omega_m) + f_{geo}(\Lambda) K_{geo}(\Omega_v, \Omega_m) \quad (3)$$

$$K_{vol} = \frac{\left(\frac{\pi}{2} - \xi\right)\cos\xi + \sin\xi}{\cos\theta_m + \cos\theta_v} - \frac{(\pi)}{4} \quad (4)$$

$$\cos\xi = \cos\theta_m \cos\theta_v + \sin\theta_m \sin\theta_v \cos\Delta\phi \quad (5)$$

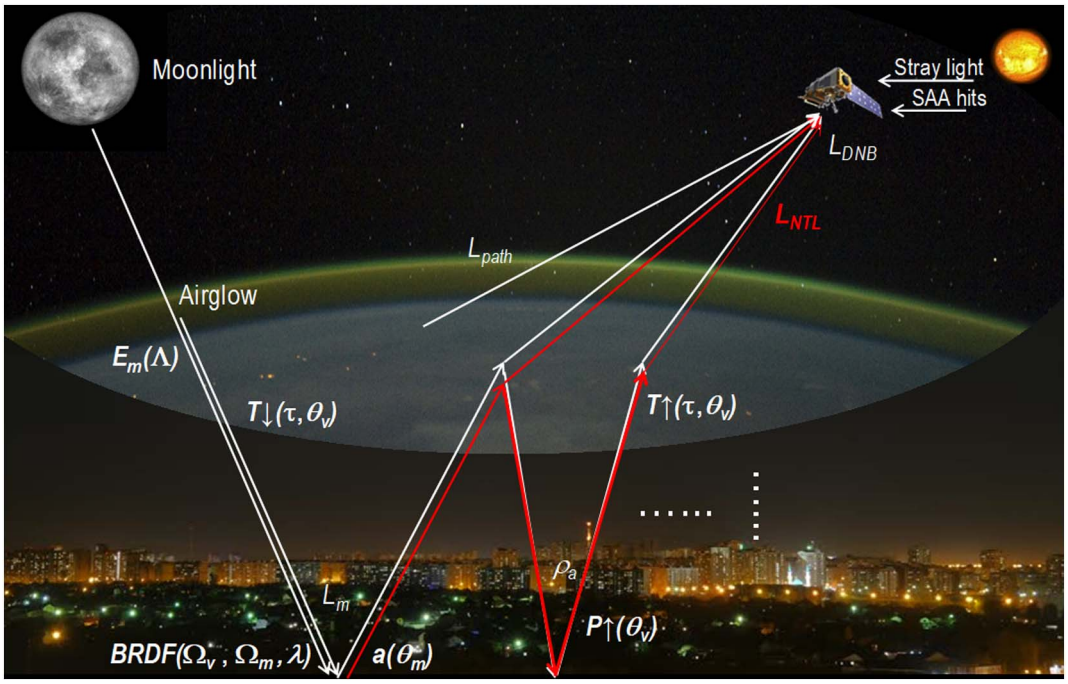

Fig. 2. Overview of NASA's Black Marble retrieval strategy (*cf.*, Eq. (1)). During the ~50% portion of the lunar cycle when moonlight is present at the time of satellite observation, the surface upward radiance from artificial light emissions, L_{NTL} [units of nWatts·cm^{-2}·sr^{-1}], can be extracted from at-sensor nighttime radiances at TOA (L_{DNB}). L_{path} is the nighttime path radiance, $a(\theta_m)$ is the VIIRS-derived actual surface albedo. The atmospheric backscatter is given by ρ_a. $T_{\downarrow}(\tau,\theta_v)$ and $T_{\uparrow}(\tau,\theta_v)$ are the total transmittances along the lunar-ground and ground-sensor paths (respectively). $P_{\uparrow}(\theta_v)$ is the probability of the upward transmission of NTL emissions through the urban vegetation canopy. Additional factors accounted for in the Level 1 process (Section 3.1) include correction for stray light and South Atlantic Anomaly (SAA) hits.

$$K_{geo} = \frac{1 + sec\,\theta'_m sec\,\theta'_v + tan\,\theta'_m tan\,\theta'_v cos\,\Delta\phi}{2} + \left(\frac{t - sin\,t\ \ cos\,t}{\pi} - 1\right)(sec\,\theta'_m sec\,\theta'_v) \quad (6)$$

$$cos^2 t = min\left\{\left(\frac{P_4}{sec\,\theta'_m + sec\,\theta'_v}\right)^2 (D^2 + (tan\,\theta'_m tan\,\theta'_v sin\,\Delta\phi)^2), 1\right\} \quad (7)$$

$$tan\,\theta'_x = P_5 tan\,\theta_x \ ; \ \ x = v \ \ or \ \ m \quad (8)$$

$$D = \sqrt{tan^2\theta'_m tan^2\theta'_v - 2\,tan\,\theta'_m tan\,\theta'_v cos\,\Delta\phi} \quad (9)$$

Here, we define the wavelength for the narrowband instrument of interest as the weighted center, Λ, of the VIIRS DNB spectral band [0.5–0.9 μm]. Parameter $f_{iso}(\Lambda)$ is the isotropic scattering component and equal to the bidirectional reflectance for a pixel viewing zenith angle $\theta_v = 0$ and a lunar zenith angle $\theta_m = 0$. Parameter $f_{geo}(\Lambda)$ is the coefficient of the LiSparse-Reciprocal geometric scattering kernel K_{geo}, derived for a sparse ensemble of surface casting shadows on a Lambertian background (Li and Strahler, 1992). Parameter $f_{vol}(\Lambda)$ is the coefficient for the RossThick volume scattering kernel K_{vol}, so called for its assumption of a dense leaf canopy (Ross, 2012). Δϕ is the relative view-sun azimuth angle ($\Delta\phi = \phi_m - \phi_v$) and ξ is the scattering phase angle between moon and view directions. The two constants, dimensionless crown relative height ($P_4 = h/b$) and shape ($P_5 = b/r$) parameters, have been fixed at $h/b = 2$ and $b/r = 1$ to invert the

Table 2
Summary statistics for Benchmark test #1; NTL (VZA, AOD). Values describe two key performance metrics for NASA's Black Marble product suite: (1) detection limit (L_{min}) and (2) robustness (L_0). Results are based on a discrete range of View Zenith Angles (VZA < 45°, VZA ≥ 45°) and Aerosol Optical Depths (AOD < 0.5, AOD ≥ 0.5) captured from all available (2012-YTD) cloud-corrected background NTL pixels for 30 VIIRS Level 3 tiles (10° × 10°).

TILE ID	Minimum detectable radiance (L_{min})				Retrieval uncertainty @ L_{min} (L_0)			
	TOA	VNP46A2	TOA	VNP46A2	TOA	VNP46A2	TOA	VNP46A2
	Moon fraction < 50%		Moon fraction ≥ 50%		Moon fraction < 50%		Moon fraction ≥ 50%	
h10v05	0.558	0.370	1.829	0.255	0.052	0.050	1.040	0.021
h11v07	0.752	0.617	2.921	0.420	0.075	0.055	1.768	0.046
h12v09	0.331	0.203	2.411	0.140	0.076	0.019	1.687	0.012
h12v10	0.322	0.188	2.340	0.127	0.077	0.016	1.668	0.012
h12v11	0.400	0.289	2.384	0.156	0.062	0.036	1.601	0.032
h13v11	0.636	0.520	2.663	0.331	0.076	0.041	1.645	0.033
h17v08	0.400	0.252	2.910	0.154	0.095	0.031	2.009	0.020
h18v04	0.692	0.540	2.162	0.355	0.069	0.157	1.211	0.055
h18v05	0.563	0.336	3.968	0.210	0.136	0.075	2.869	0.013
h19v04	0.763	0.610	2.223	0.419	0.088	0.091	1.248	0.089
h20v11	0.336	0.221	2.475	0.124	0.065	0.022	1.734	0.023
h21v05	0.641	0.435	3.255	0.279	0.065	0.042	2.158	0.031
h22v05	0.714	0.535	3.398	0.319	0.077	0.032	2.229	0.043
h22v06	0.581	0.440	4.572	0.255	0.117	0.028	3.399	0.034
h23v05	0.543	0.350	2.844	0.208	0.073	0.040	1.964	0.027
h23v06	0.595	0.451	3.954	0.269	0.131	0.033	2.918	0.033
h24v05	0.446	0.226	2.963	0.129	0.070	0.039	2.132	0.024
h24v06	0.428	0.254	2.983	0.145	0.090	0.042	2.190	0.029
h25v05	0.517	0.296	3.023	0.169	0.045	0.047	2.055	0.018
h25v06	0.647	0.484	2.994	0.293	0.079	0.058	1.959	0.030
h25v07	0.641	0.521	2.715	0.317	0.076	0.048	1.725	0.032
h25v08	0.501	0.413	2.181	0.268	0.081	0.039	1.408	0.031
h26v05	0.425	0.206	3.142	0.110	0.092	0.040	2.335	0.019
h26v06	0.568	0.405	2.682	0.233	0.080	0.057	1.740	0.028
h26v07	0.428	0.326	2.051	0.188	0.067	0.041	1.325	0.026
h27v05	0.416	0.191	3.001	0.098	0.072	0.034	2.215	0.016
h27v06	0.410	0.241	2.494	0.122	0.066	0.037	1.733	0.023
h28v08	0.457	0.342	2.515	0.241	0.055	0.028	1.686	0.025
h29v05	0.580	0.359	2.379	0.204	0.058	0.053	1.444	0.022
h32v12	0.290	0.153	2.262	0.076	0.074	0.029	1.692	0.021

angular radiance data from the VIIRS DNB (Wanner et al., 1997). For these two parameters, h is the variable for height at which a crown center is located, b is the vertical half axis of the modeled ellipsoid, and r is its horizontal radius. In Eq. (2), d is the Earth-Sun distance $E_m(\Lambda)$ [units of $nW{\cdot}m^{-2}$] is the downwelling TOA sensor response function-weighted lunar irradiance (Miller and Turner, 2009), and *BRF* is the surface bidirectional reflectance factor – the ratio of the BRDF to that of a perfect Lambertian reflector (*i.e.*, BRF ≈ πBRDF) (Nicodemus, 1977; Schaepman-Strub et al., 2006).

To achieve a high-quality BRDF retrieval, the NASA Black Marble algorithm collects all available daytime, atmospherically-corrected, VIIRS DNB BRFs over a multi-date period (normally 16-days) to establish the analytical solution for the Ross-Li BRDF model parameter values, $f_k(\Lambda)$. Note that during moon-free nights, when atmospheric air glow is the dominant emission source, the VNP46 algorithm sets the illumination geometry to near-nadir ($\theta_m = 10^{\circ}$) and the Lunar Irradiance to $E_m(\Lambda) = 0.26\ nW{\cdot}m^{-2}$ (Liao et al., 2013). This enables a BRDF correction even in the absence of moonlight.

2.3. Seasonal vegetation correction

Another known source of uncertainty in the retrieval of satellite-derived NTL is the influence of canopy-level foliage along the ground-to-sensor geometry path (Román and Stokes, 2015). This effect, which has been shown to reduce the magnitude of NTL at city-wide scales (Levin, 2017; Levin and Zhang, 2017), is most pronounced in temperate urban regions; where mixed and deciduous vegetation are most pervasive. Given its seasonal dependence, this occlusion effect (obscuration of surface light by foliage) should be proportional in magnitude to the density and vertical distribution pattern of leaves within a given VIIRS DNB pixel. Hence, while the effect may be non-linear (due to the confluence of factors that control the seasonality, physiognomy, and vertical distribution of urban vegetation canopies), the effect can be parameterized using analytical models which aim to retrieve canopy structure parameters from multi-angle remote sensing data (Chopping, 2006). With this concept in mind, we are employing a vegetation dispersion parameter, known as the clumping index, ψ, to parameterize the confined distribution of foliage within distinct canopy structures (Chen et al., 2005; Chen and Black, 1991; Jiao et al., 2018; Leblanc et al., 2005; Nilson, 1971):

$$P_{\uparrow}(\theta_v) = e^{-\psi G(\theta_v) LAI / \cos(\theta_v)} \quad (10)$$

Here, $P_{\uparrow}(\theta_v)$ is the probability of the upward transmission of NTL emissions through the urban vegetation canopy (known as the gap fraction probability and hereafter termed the P_{gap} equation), $G(\theta_v)$ is the extinction coefficient that expresses the mean area projection of plant elements in the direction θ_v (being 0.5 for canopies with a random distribution of leaf angles), and *LAI* is the Leaf Area Index. If $LAI = 0$, then $P_{\uparrow}(\theta_v) = 1$ and a correction is not performed. When $LAI > 0$, and foliage grouping has a random distribution, then the clumping index $\psi = 1$ and Eq. (10) returns to the original Beer's law. The latter includes areas with single ground-layers (*e.g.*, peri-urban vegetation).

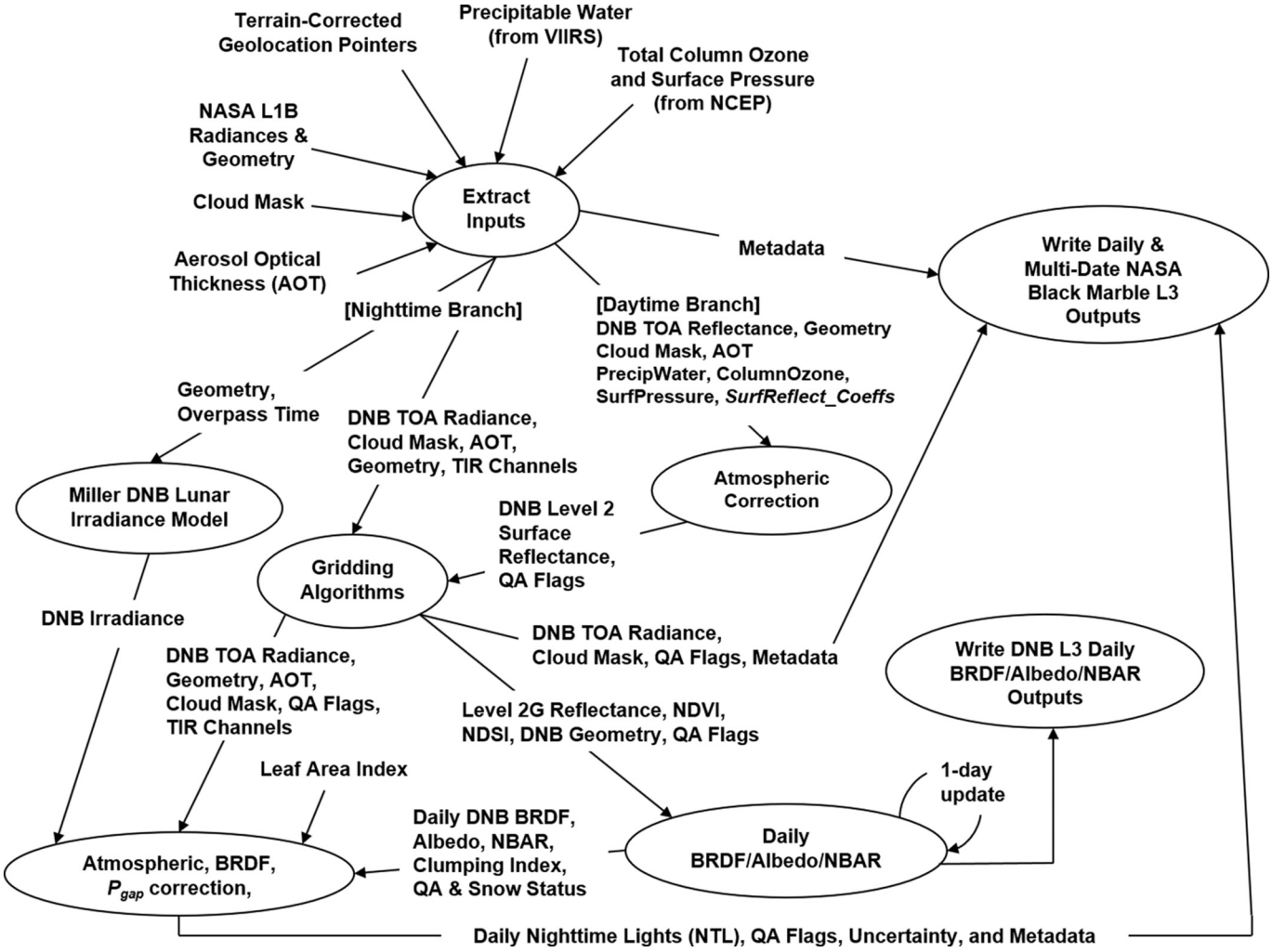

Fig. 3. Algorithm processing cycle and ancillary parameters used by NASA's Black Marble product suite (VNP46).

Conversely, if the distribution is not random, then the clumping index can be larger or smaller than unity. In the case that the leaf distribution is more regular (leaves side by side) than random, then the clumping index $\psi > 1$. As such, the same value of *LAI* over a given VNP46 pixel, can intercept more NTL emissions originating from the ground surface; thus, making $P_{\uparrow}(\theta_v)$ smaller, and the corresponding adjustment to L_{NTL} ($P_{\uparrow}(\theta_v)$ in Eq. (1)) is larger.

The P_{gap} equation can be inverted from available daily VIIRS BRDF-derived clumping index values, as done in Hill et al. (2011) and He et al. (2012). The VIIRS LAI retrievals are based on the current standard product (VNP15) (Park et al., 2017). In the case of poor-quality or missing LAI values (*e.g.*, when LAI is not retrieved over dense urban areas), we are employing the VIIRS LAI backup algorithm by using a Look-up Table (LUT) (Knyazikhin et al., 1999; Xiao et al., 2016) with Normalized Difference Vegetation Index (NDVI) generated from high quality retrievals from the VIIRS NBAR product (Shuai et al., 2013). Using this approach, we can define the clumping index based on Chen et al. (2005) as:

$$\psi = \boldsymbol{C}(\theta_v)\boldsymbol{NDHD}(\boldsymbol{\Omega_v}, \boldsymbol{\Omega_m}, \boldsymbol{\Lambda}) + \boldsymbol{D}(\theta_v) \quad (11)$$

$$\boldsymbol{NDHD}(\boldsymbol{\Omega_v}, \boldsymbol{\Omega_m}, \boldsymbol{\Lambda}) = \frac{\boldsymbol{BRF_{hot}}(\boldsymbol{\Omega_v}, \boldsymbol{\Omega_m}, \boldsymbol{\Lambda}) - \boldsymbol{BRF_{dark}}(\boldsymbol{\Omega_v}, \boldsymbol{\Omega_m}, \boldsymbol{\Lambda})}{\boldsymbol{BRF_{hot}}(\boldsymbol{\Omega_v}, \boldsymbol{\Omega_m}, \boldsymbol{\Lambda}) + \boldsymbol{BRF_{dark}}(\boldsymbol{\Omega_v}, \boldsymbol{\Omega_m}, \boldsymbol{\Lambda})} \quad (12)$$

Here, *NDHD* is the Normalized Difference between Hotspot and Darkspot (NDHD) – an angular index used to characterize the anisotropic behavior of vegetation, which has been related to ground based measurements of clumping index (He et al., 2012; Jiao et al., 2016, 2018; Lacaze et al., 2002; Leblanc et al., 2005; Zhao et al., 2012). BRF_{hot} and BRF_{dark} are the reflectances at the 'hotspot' and 'darkspot', respectively. Thus, NDHD can be estimated directly from the retrieved VIIRS BRDF model parameters (f_{iso}, f_{vol}, f_{geo} in Eq. (3)) by specifying the RTLSR model kernels for the corresponding hotspot and darkspot geometries. The values of C (θ_v) and D (θ_v) in Eq. (1) are estimated by applying the linear coefficients of the line of best fit to the VIIRS-derived NDHD values (see Table 2 in Chen et al., 2005). For the VNP46 implementation, we chose the coefficients of regression based on a full ellipsoid shape in the Red spectral region [0.662–0.682 μm]. The P_{gap} effect is dominant across NTL pixels with lower build-up densities (*e.g.*, small cities and suburban areas), where green spaces are often protected from development. In contrast, P_{gap} values are often closer to unity (no correction) near densely built city centers.

3. Product generation

3.1. Level 1 calibrated DNB radiances

The VIIRS DNB sensor is a temperature controlled Charge Coupled Device (CCD) that has 672 sub-pixel detectors along-track, which are aggregated on-board to create 16 nearly constant 742 m along-track pixels for each along-scan frame (Wolfe et al., 2013). These observations are acquired at three different stages of Low- Mid- and High-Gain (LGS, MGS, and HGS, respectively) with high sensitivity for low NTL conditions (Mills and Miller, 2016). With the aggregation mode, detector, gain stage, and Half-angle Mirror (HAM)-side dependent calibration performed, the VIIRS DNB degradation was conclusively traced

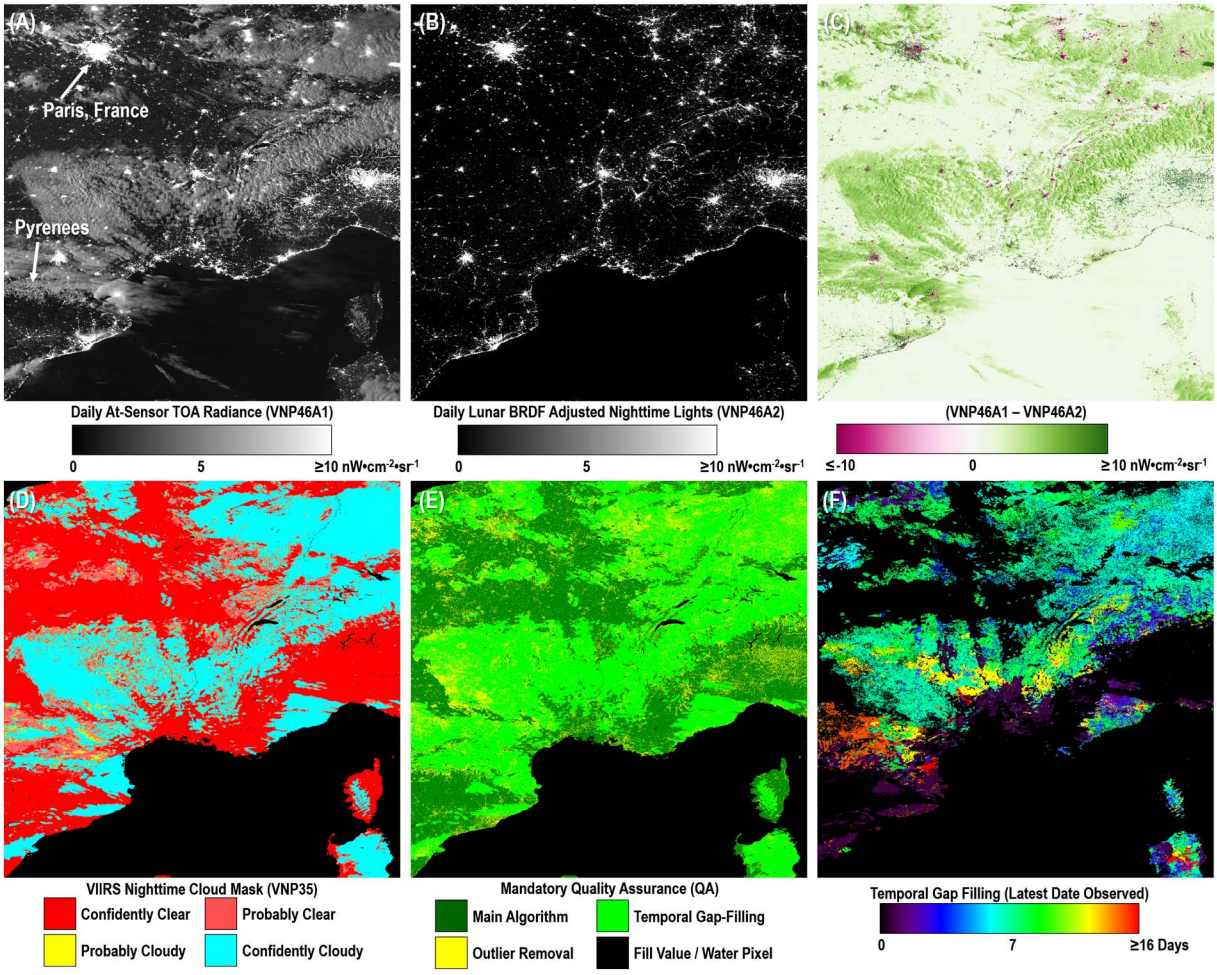

Fig. 4. VNP46 product suite components for a 10° × 10° Level 3 tile over France and the Balearic Sea region (h18v04; DOY 2015-091). The full-moon-illuminated and 51% cloud-contaminated scene illustrates the challenges of nighttime cloud masking over snow-covered surfaces (*e.g.*, the French Alps and the Pyrenees).

and has been well characterized (Chen et al., 2017; Xiong et al., 2014). The stray light contamination on the DNB, which is a transient issue affecting up to 25% of night scenes in the mid-to-high latitude regions (Chen et al., 2017; Mills et al., 2013), is also being routinely corrected by the VIIRS Calibration Support Team (VCST) (Chen et al., 2017; Lee et al., 2014). Results from ongoing collection V001 reprocessing of the NASA Level 1 product include additional updates to the VIIRS DNB terrain-corrected geolocation, stray light, and calibration LUTs. Finally, routine reporting and removal of bad DNB granules (*e.g.*, resulting from Suomi-NPP calibration maneuvers or Rotating Telescope Assembly (RTA)/HAM sync loses) is being conducted by the VCST using specialized software to mitigate leakage into the VNP46 product suite.

3.2. Algorithm processing cycle

NASA's Black Marble (VNP46) algorithm processing cycle is divided into daytime and nighttime branches (Fig. 3). Each processing branch produces a unique set of ancillary and quality assurance (QA) flags.

For the daytime branch, science product generated executables (PGEs) based on the standard suite of VIIRS Land products are integrated as part of NASA's Black Marble processing chain. First, a modified version of the operational VIIRS Surface Reflectance algorithm (Roger et al., 2016; Vermote et al., 2014) is used to generate the DNB surface bi-directional reflectances (BRFs) using NASA's Level 1B calibrated radiance product as input (*i.e.*, 6-minute granules, or 2366 km along track and ~3100 km across-track). Level 2G DNB Surface Reflectances are then generated by performing spatial and temporal aggregation to 500 m grid cells over daily time periods (Campagnolo et al., 2016; Pahlevan et al., 2017; Wolfe et al., 1998; Yang and Wolfe, 2001). Daily Level 3 DNB BRDF/Albedo data are then retrieved using the heritage MODIS/VIIRS algorithm (MCD43/VNP43) (Liu et al., 2017, 2017; Wang et al., 2018), and corresponding Snow Flags are estimated using the heritage VIIRS Normalized Difference Snow Index (NDSI) algorithm (VNP10) (Riggs et al., 2016, 2017). The NDVI and NDSI values are used to determine the growing, dormant, and snow periods to routinely update the *a priori* global database of the DNB BRDF product (Cescatti et al., 2012; Liu et al., 2017, 2017; Román et al., 2009). Surface BRFs from the VIIRS I1 (red) and I2 (NIR) channels are used to obtain daily estimates of LAI (Knyazikhin et al., 1999; Park et al., 2017; Xiao et al., 2016). The retrieved LAI and clumping index values are then used to calculate the gap fraction probability (P_{gap}).

The nighttime branch describes the path followed to generate the final VNP46 products. We begin with the at-sensor TOA nighttime radiances (VNP46A1), along with the corresponding nighttime cloud mask, multiple Solar/Viewing/Lunar geometry values (including moon-illuminated fraction and phase angles), and the daily snow and aerosol status flags. These additional Science Data Sets (SDS) enable open access to the primary inputs used to generate the NASA Black Marble NTL time series record; thus, ensuring reproducibility of the final outputs. For example, using VNP46A1 as input, end-users seeking to employ NTL data in light pollution studies can develop different variations of the products under different sky-illumination conditions (*e.g.*, daily retrievals in which atmospheric, topographic and cloud effects are

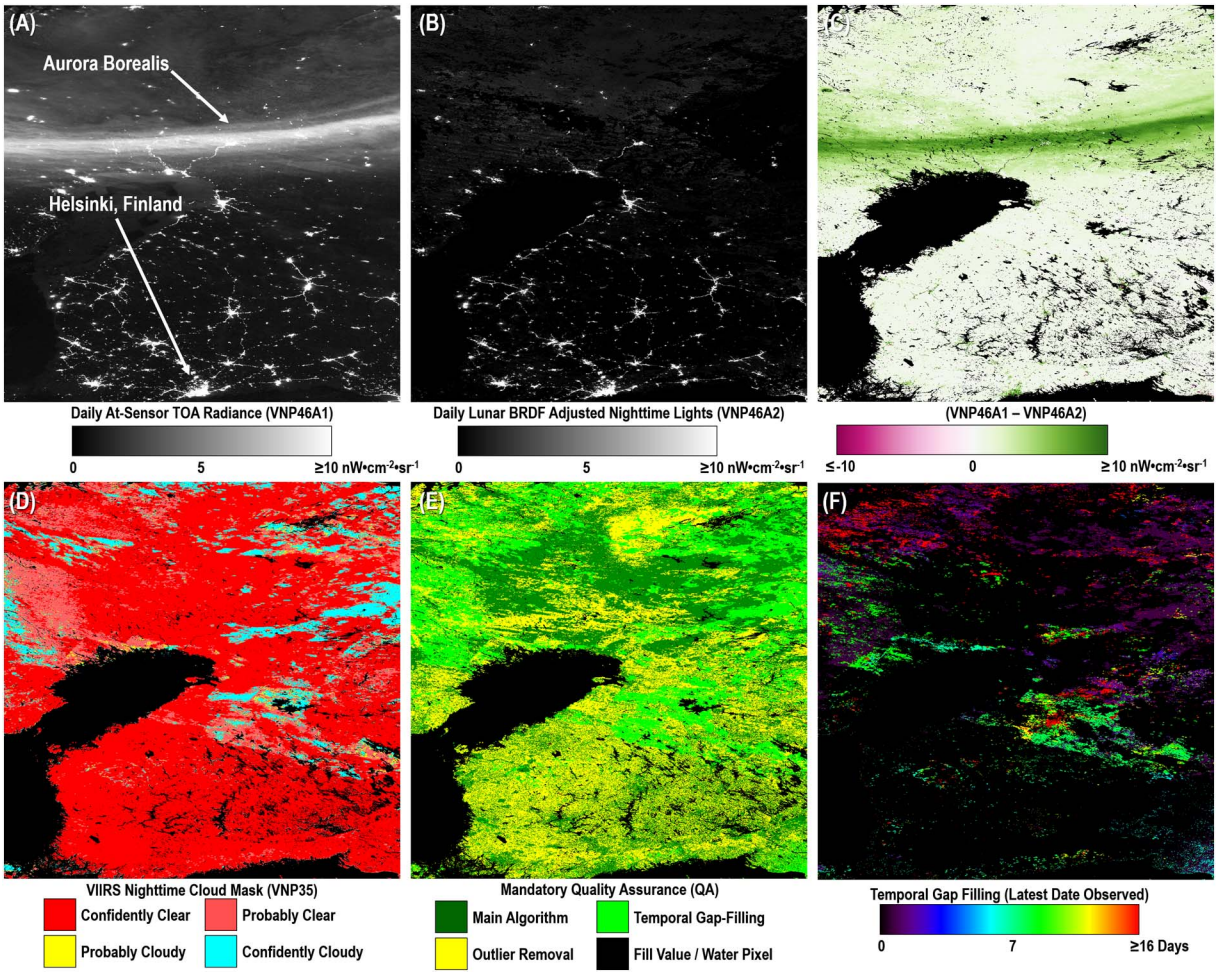

Fig. 5. VNP46 product suite components for a 10° × 10° Level 3 tile over Sweden and Finland (h20v02; DOY 2013-080). The half-moon-illuminated and 30% cloud-contaminated scene is shown to capture extraneous light emissions north of the Gulf of Bothnia caused by the Aurora Borealis.

removed, but seasonal and lunar-related changes are not removed). Algorithm developers also interested in contributing additional refinements to the VNP46 product suite, or in developing their own series of higher-level DNB products (*e.g.*, for nighttime aerosol, cloud optical properties, and ocean NTL applications), can also make use of these SDS layers; thus, greatly reducing the complexity of science data processing.

A series of temporal and spatial gap-filling techniques are also employed to improve the coverage of the VNP46 NTL product. The approach, based on the asymmetric Gaussian fitting method from the TIMESAT package (Jönsson and Eklundh, 2002, 2004; Tan et al., 2011) and used by the heritage MODIS BRDF/Albedo/NBAR, land surface phenology, and LAI product suites (Gao et al., 2008; Sun et al., 2017; Tan et al., 2008), is also applied to the VIIRS DNB BRDF model parameters (to calculate the appropriate gap-filled albedo values) and the corresponding P_{gap} values.

Results shown in Figs. 4 and 5 illustrate the key processing steps used to retrieve high-quality NTL as part of NASA's Black Marble product suite. Cloud-free, atmospheric-, seasonal-, and moonlight BRDF-corrected DNB nighttime radiances are produced using the nighttime DNB Level 1 at-sensor radiances, nighttime cloud mask, aerosol optical

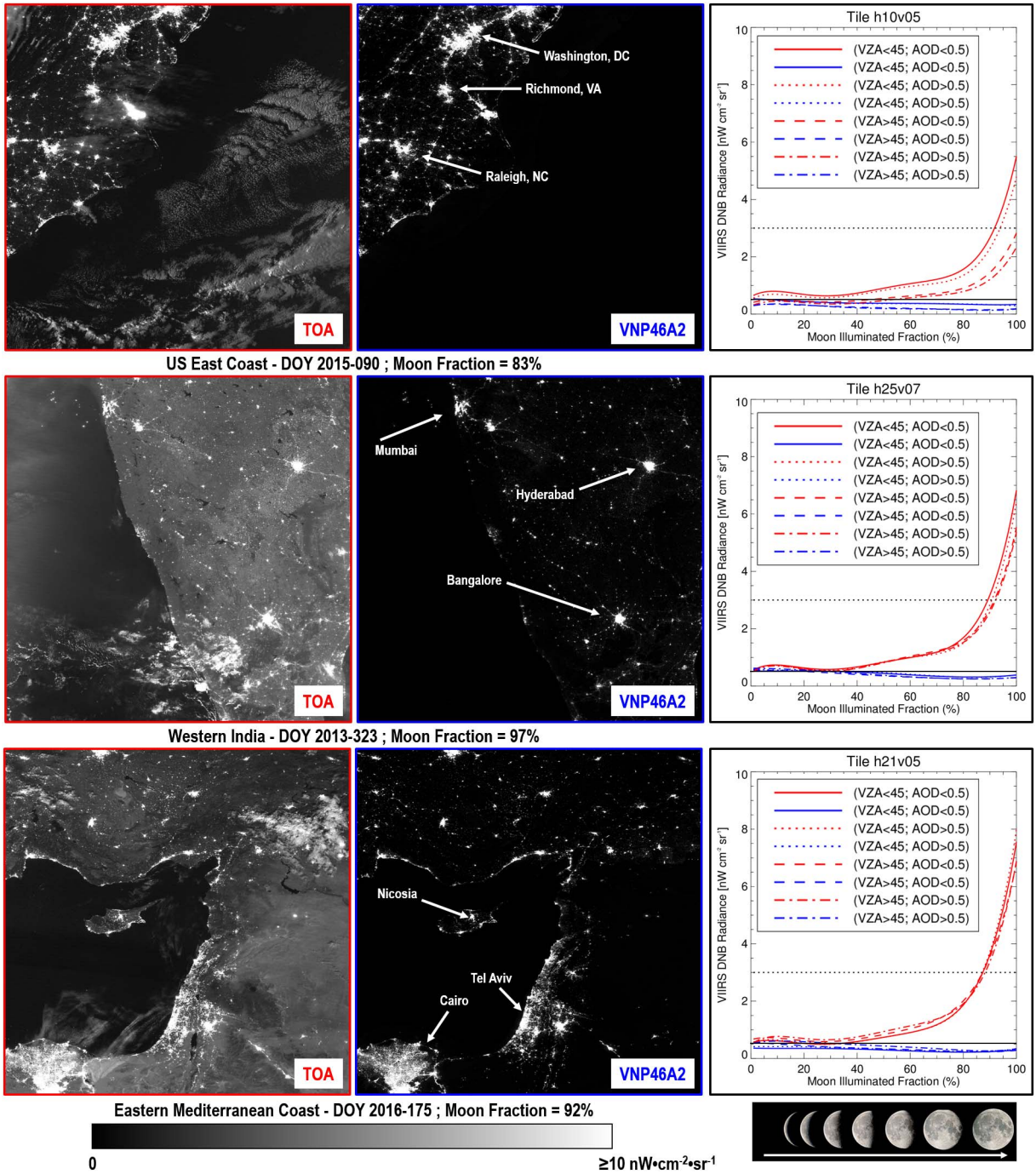

Fig. 6. Benchmark test #1: NTL (View Zenith Angle (VZA), Aerosol Optical Depth (AOD). (Left and Center) Daily VIIRS TOA (cloud-corrected at-sensor DNB radiances in nW·cm^{-2}·sr^{-1}) and VNP46A2 scenes (cloud-free, atmospheric-, seasonal-, and moonlight BRDF-corrected DNB nighttime radiances) are shown in red and blue (respectively) for three Level 3 tiles exhibiting near- to full-moon conditions. Cloudy pixels were left visible in the TOA product for viewing purposes. (Right) Benchmark test #1 plots corresponding to each scene. For reference, the threshold (L_{min} = 3.0 nW·cm^{-2}·sr^{-1}) and breakthrough (L_{min} = 0.5 nW·cm^{-2}·sr^{-1}) performance specifications are shown as black-dotted and solid horizontal lines (respectively). (For interpretation of the references to colour in this figure legend, the reader is referred to the web version of this article.)

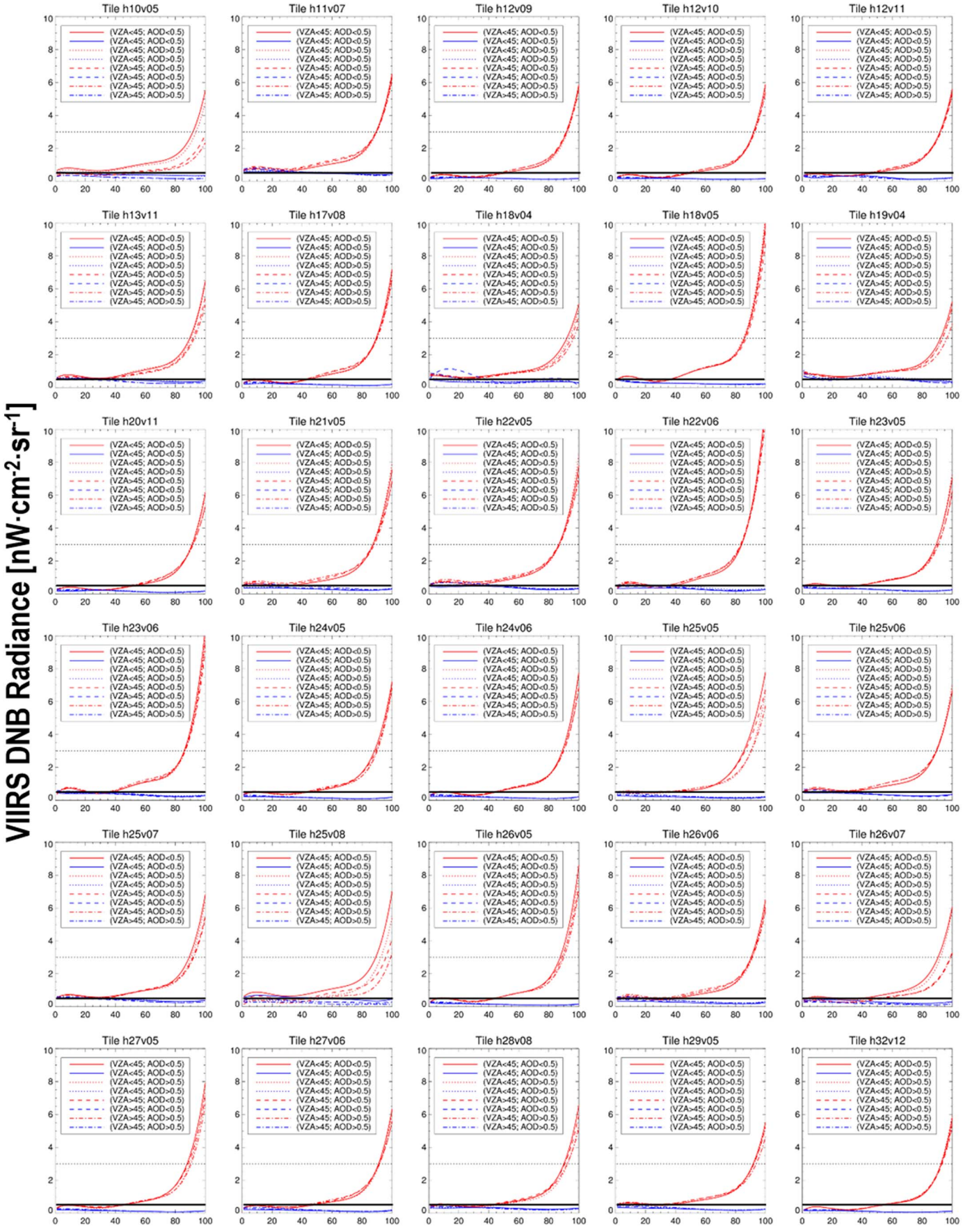

(caption on next page)

Fig. 7. Results for Benchmark test #1: NTL (VZA, AOD). A globally representative spatial sample of 30 VIIRS Level 3 tiles provides insights into the performance of the NASA Black Marble NTL radiance product (VNP46A2: shown in blue) compared to cloud-corrected at-sensor radiances (TOA: shown in red) (both shown in units of $nW{\cdot}cm^{-2}{\cdot}sr^{-1}$). Results are plotted along the full range of illumination conditions experienced by the DNB time series record (X-axis = Moon Illuminated Fraction %). For reference, the threshold (L_{min} = 3.0 $nW{\cdot}cm^{-2}{\cdot}sr^{-1}$) and breakthrough ($L_{min}$ = 0.5 $nW{\cdot}cm^{-2}{\cdot}sr^{-1}$) performance specifications are shown as black-dotted and solid horizontal lines (respectively). (For interpretation of the references to colour in this figure legend, the reader is referred to the web version of this article.)

depth values, snow status flag, Ross-Li DNB BRDF model parameters and albedo values, P_{gap}, and per-pixel estimates of DNB Lunar irradiance and corresponding geometries. A mandatory quality assurance (QA) flag is then provided to establish the pixel-specific estimates of retrieval performance. Note that, when the temporal gap-filling routine is called upon, as reported in the Mandatory Quality Assurance (QA) Flags (Table A4), the latest high-quality date observed, based on retrievals using the main algorithm, is reported as a separate SDS layer. If an outlier is still detected after temporal gap-filling, then the VNP46 algorithm defaults to a monthly climatology based on the most recent available moonless high QA values. Thus, through judicious use of the VNP46 product quality flag, the end-user can establish whether a particular temporally-gap filled NTL value is based on a recent date or not. This results in a traceable moonlight-adjusted NTL product to assess current *versus* recent NTL conditions, while reducing persistent data gaps caused by nighttime clouds, snow, and other ephemeral artifacts (*e.g.*, the Aurora Borealis - *cf.*, Fig. 5). The reader is referred to the Appendix for additional details regarding the individual VNP46 products, including a full description of quality flags and controls exercised through the NTL retrieval process.

4. Evaluation of product performance

The overarching goal of NASA's Black Marble science product development efforts is to achieve a “Breakthrough” performance specification (*cf.*, Table 1) by conducting the following tasks: (1) long-term stability monitoring of the entire VNP46 algorithm processing chain, including the fundamental (Level 1B) VIIRS DNB time series record, terrain-corrected geolocation, stray light correction, and calibration LUTs; and (2) global quality assessment, uncertainty quantification, and product validation. To assess progress on these tasks, we have developed a series of seven benchmark tests to quantify product performance at representative spatial and temporal scales. This comprehensive suite of benchmark tests and assessment metrics is meant to ensure that variations in VNP46 product performance can be identified quickly, so that improvements can be implemented in a timely fashion. It also enables the end-user to consider the products in their appropriate context, *e.g.*, by anticipating appropriate noise reduction levels under specific retrieval conditions.

4.1. Detection limit and robustness

To enable quantitative uses of NTL time series data, one must first establish the robustness of the algorithm with appropriate detection limits that are globally applicable and temporally consistent. This is particularly true when using NTL to characterize abrupt short-term changes (*e.g.*, power outages) or to quantify low-lit NTL across areas of concentrated energy poverty (see examples in Figs. 15–16). Accordingly, we conducted a series of benchmark tests to address the following questions:

- Benchmark test #1: How do daily variations in aerosol optical depth, under varying view-illumination conditions, influence NTL retrieval performance?
- Benchmark test #2: How do daily variations in surface albedo, under varying view-illumination conditions, influence NTL retrieval performance?
- Benchmark test #3: Is there a dependence between NTL and daily variations in anisotropic diffuse moon-illumination and multiple scattering (*i.e.*, albedo-aerosol coupling effects)?

The goal of benchmark tests #1 to #3 is to assess variations in low-lit NTL emissions; hereby expressed in terms of the background noise, or floor, of a NTL product; where both L_{min} and L_0 should equal to 0.0 $nW{\cdot}cm^{-2}{\cdot}sr^{-1}$. For each benchmark test, we employed a large spatial sample of 30 Level 3 tiles (each sized: 10° × 10° - *cf.*, highlighted red tiles in Fig. 17) using the entire available VIIRS DNB (Collection V001) time series. This augmented analysis was necessary to capture a diverse range of geographic locations and time periods representing global conditions. To further establish whether a correction resulted in improved performance, each benchmark test was conducted at two different levels of the NASA Black Marble algorithm processing chain: (1) at the upstream level, using cloud-corrected at-sensor TOA radiances (hereby termed, TOA), and (2) at the final processing level; using cloud-, atmospheric-, seasonal-, and moonlight BRDF-corrected NTL data (VNP46A2).

We used the following sampling scheme to produce statistical metrics for each benchmark test: (1) Background NTL pixels contained within each sampled Level 3 tile (30 in total) were identified using the Global Urban Footprint (GUF) product (Esch et al., 2013, 2017) and removing 1% of outliers. (2) The samples were partitioned into 12 groupings, each representing a discrete range of daily black-sky albedo (BSA, BSA < 0.2, BSA ≥ 0.2), viewer zenith angle (VZA, VZA < 45°, VZA ≥ 45°), and aerosol optical depths (AOD, AOD < 0.5, AOD ≥ 0.5) (see plot legends in Figs. 6–11). (3) For each of these groupings, the average TOA and VNP46A2 radiance was estimated for instances with matching illumination conditions. (4) Finally, each of these instances was then paired with sample data from the entire available DNB time series record (2012–mid 2017), corresponding to the full range of illumination conditions (*i.e.*, average values for samples with moon illuminated fractions from 0% to 100%, with a precision of ± 1.5°). Results for benchmark tests #1 to #3 (Figs. 6–11), as well as summary statistics extracted for four final groupings (*i.e.*, TOA *vs* VNP46A2, for moon illuminated fraction < 50% and moon illuminated fraction ≥50%) (Tables 2–4), illustrate the highly non-linear dependence of background DNB pixels to BSA, VZA, AOD, and combinations thereof.

The individual (tile-based) benchmark test results in Figs. 7, 9, and 11 (which plot background NTL pixels as a function of moon-illuminated fraction) help illustrate how the refined product (VNP46A2) maintains a near constant background radiance profile across the entire lunar illumination cycle; well within the “Breakthrough” and the “Goal” performance requirements for L_{min} and L_0, respectively. In contrast, when using the cloud-corrected TOA product, only 27% of reported cases (all based on moonless periods, where Moon Fraction < 50%) met the “Goal” requirement, while 37% of cases (all based on moonlit conditions, where Moon Fraction ≥50%) failed to meet the minimum “Threshold” requirement; indicating the TOA product's lack of consistency (in a global sense), and its inaptness for applications requiring a stable NTL time series record for accurate characterization of change.

The albedo effect is shown to significantly influence NTL product performance, particularly during moonlit periods (Moon Fraction ≥50%). For most VIIRS Level 3 tiles, L_{min} values for TOA data with albedos < 0.2 were consistently lower than values with BSA data higher than 0.2. For TOA products during moonlit periods, the influence of albedo was also more pronounced compared to AOD. Both the detection limit (L_{min}) and robustness (L_0) were also found to be larger (and therefore worse) over desert regions, *e.g.* the Saharan Desert (h18v05), the Middle East (h21v05, h22v05, h22v06, and h23v06), and the Tibetan Plateau (h26v05, h26v06, h27v05, and h27v06). For these cases, L_{min} and L_0 often failed to meet their “Threshold” performance requirements. While the increased level of measurement error in the

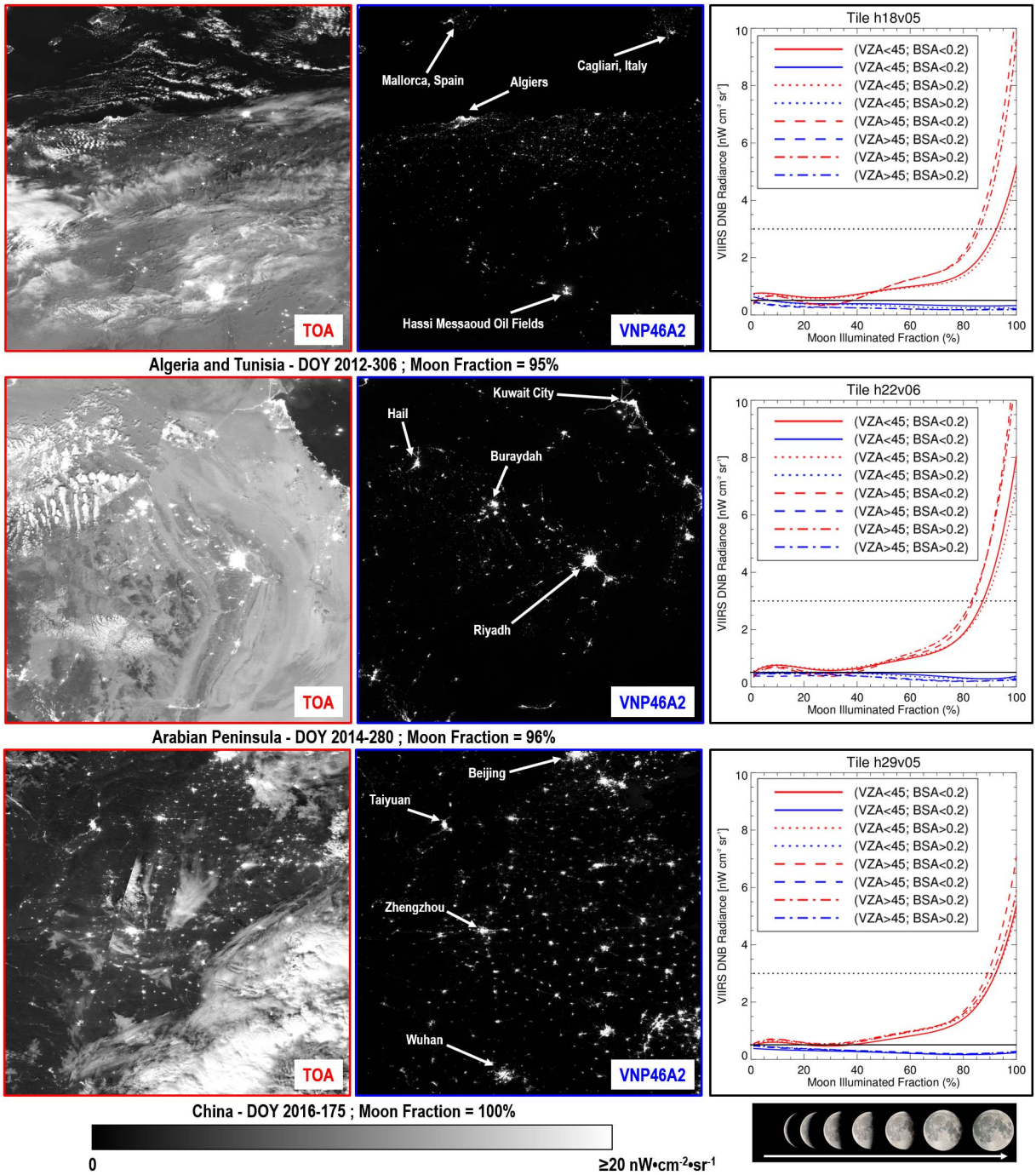

Fig. 8. Benchmark test #2: NTL (VZA, BSA). Note the dynamic range used for the Daily TOA and VNP46A2 scenes (Left and Center) is [0 to 20 nWatts·cm^{-2}·sr^{-1}]. Otherwise, setup is the same as Fig. 6.

TOA data can be anticipated for bright surface conditions, the fact that equally higher degradations for L_0 were observed suggests that additional higher-order effects (*e.g.*, increased influence of anisotropic diffuse illumination and multiple scattering) are also impacting NTL retrieval quality. This was especially true for desert areas, where the total uncertainty of the product ($L_{min} + L_0$) is shown to be higher than the L_{min} "Threshold" performance requirement by a factor of at 1.6× to 2.0×.

We also found that the restricted use of TOA data under moonless nights does not necessarily result in a higher-quality NTL retrieval; even for conditions experiencing lower AOD and albedos (Figs. 7 and 9). In fact, 98.3% of VNP46A2 benchmark test results under moonlit conditions, for both L_{min} and L_0, were actually lower (and thus better) than the TOA benchmark test results under moonless conditions (Tables 2, 3, and 4). These benchmark tests, therefore, help confirm the temporal consistency of the VNP46A2 product across the entire moon-illuminated cycle.

4.2. Performance of the VIIRS nighttime cloud mask

Another key factor that affects the quality of NTL products is the performance of the VIIRS Nighttime Cloud Mask (VCM). Accordingly, we conducted the following benchmark test to establish the following question:

- Benchmark test #4: What is the fraction of confidently clear land-

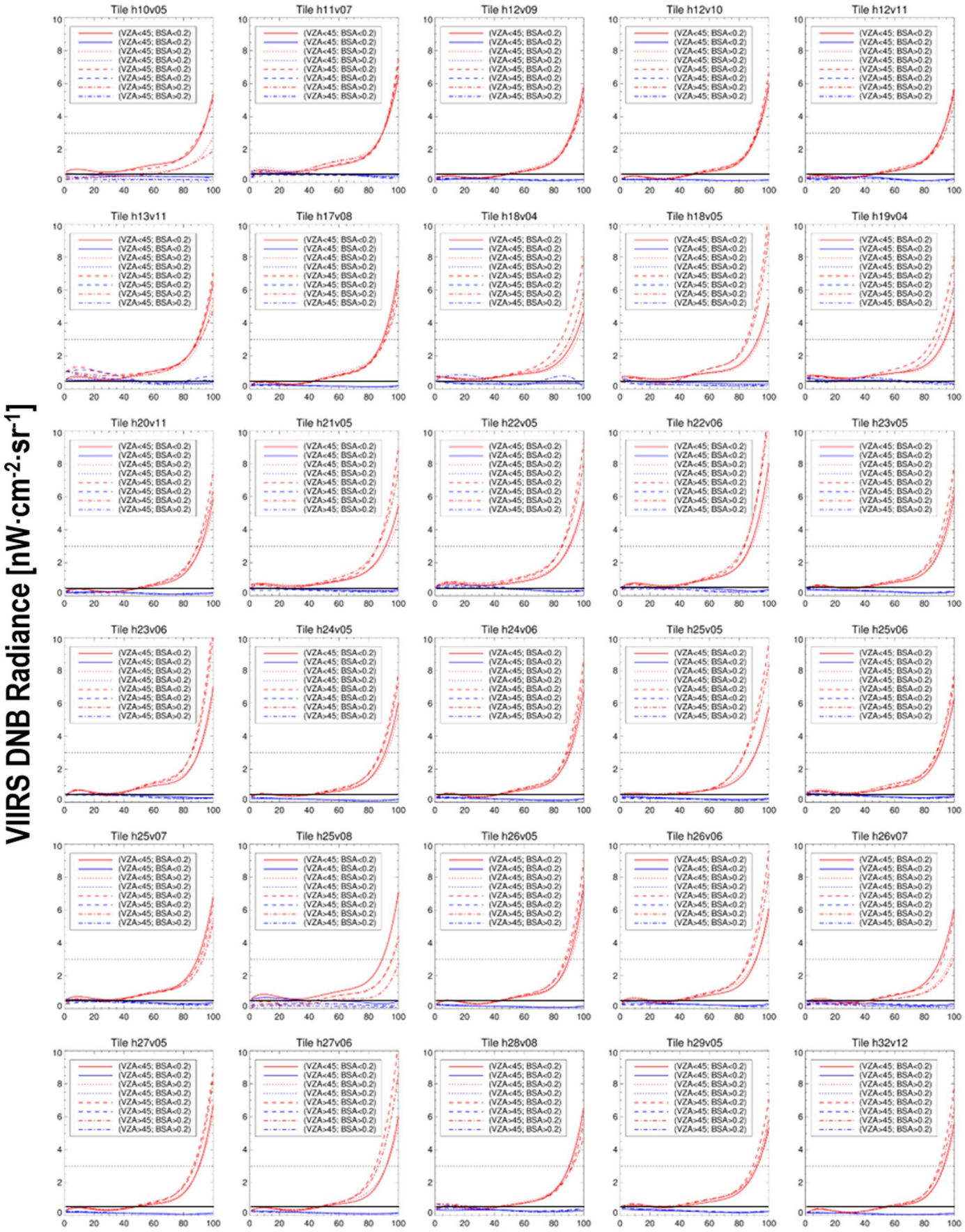

Fig. 9. Results for benchmark test #2: NTL (VZA, BSA). Set up is the same as Fig. 7.

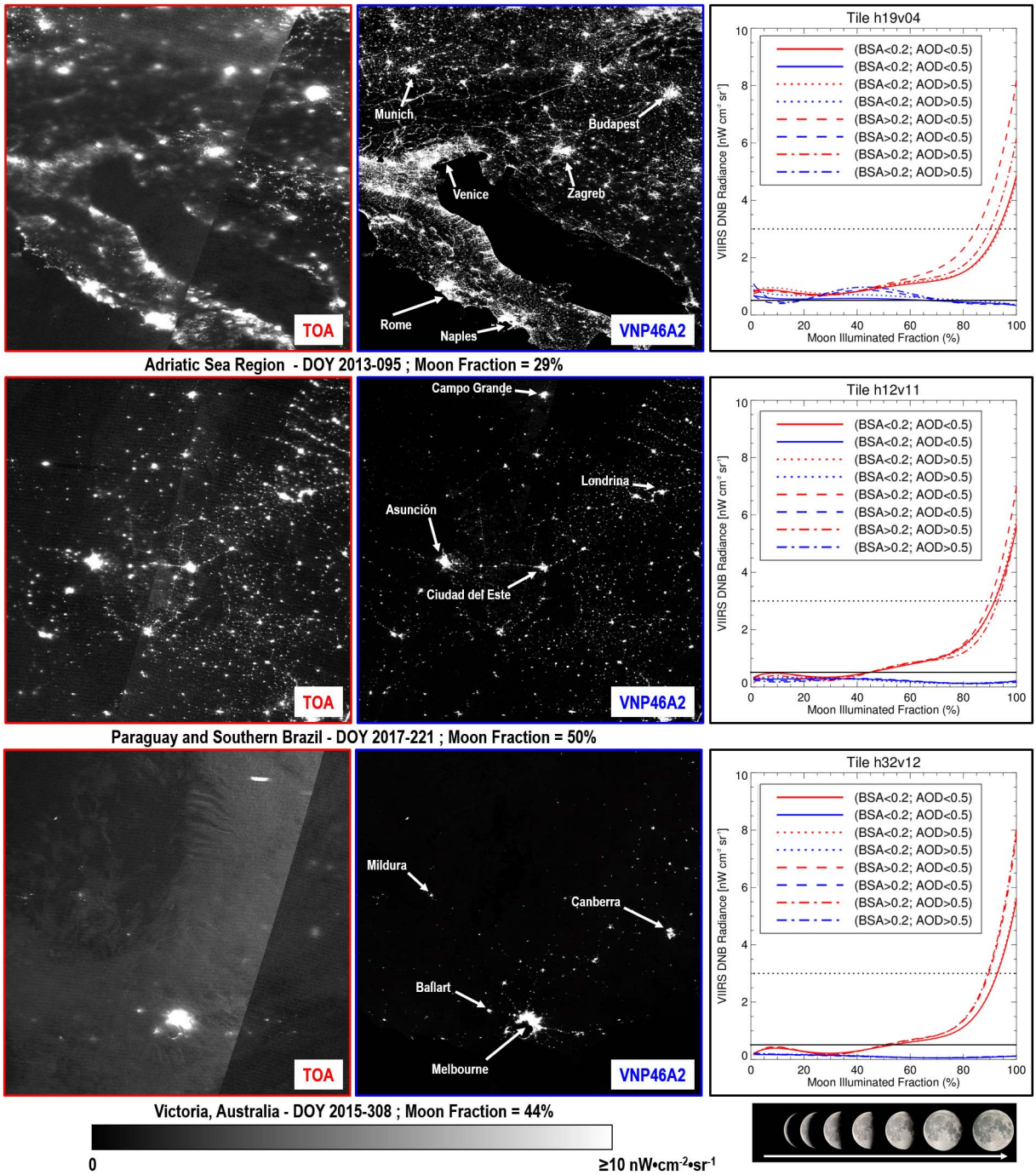

Fig. 10. Benchmark Test #3: NTL (BSA, AOD). Note the Daily TOA and VNP46A2 scenes (Left and Center) exhibit half-moon to moonless conditions (Moon Fraction ≤50%). Otherwise, setup is the same as Fig. 6.

based nighttime VCM detections that were flagged by the VNP46 algorithm as less than a high-quality NTL retrieval?

The goal of this test is to establish the overall skill of the VCM to correctly map confidently clear nighttime pixels, which (in the absence of additional post-processing steps) can lead to a high-quality NTL retrieval. The performance metric is expressed in terms of the probability of correct typing (PCT) (Kopp et al., 2014). We established PCT values by counting the total number of confidently clear VCM pixels that were subsequently flagged for additional inspection. Flagging of suspect VCM detections is done in the Lunar BRDF correction process (nighttime branch, Section 3.2), which outputs a poor-quality mandatory QA flag when the VNP46 algorithm fails to produce a reliable NTL result, and through additional consistency checks conducted during the temporal gap-filling process.

Results for benchmark tests #4 (Tables 5-6) illustrate how the performance of the nighttime VCM varies significantly depending on factors such as moon-illumination conditions, surface albedo (*e.g.*, retrieval conditions with high albedos, *e.g.*, desert and snow have worst PCT values), as well as atmospheric, climatic, and geographic conditions. The VCM performance requirement established by the JPSS program is ≥88% PCT. This requirement only applies to thick clouds optical thickness (COT) > 1.0 tau. This is a challenge for NTL time series detection, particularly since thin cirrus and low cloud fields often lead the VCM to think that the NTL pixel is clear. In addition to NTL attenuation caused by clouds with COT values < 1.0 tau, the scattering

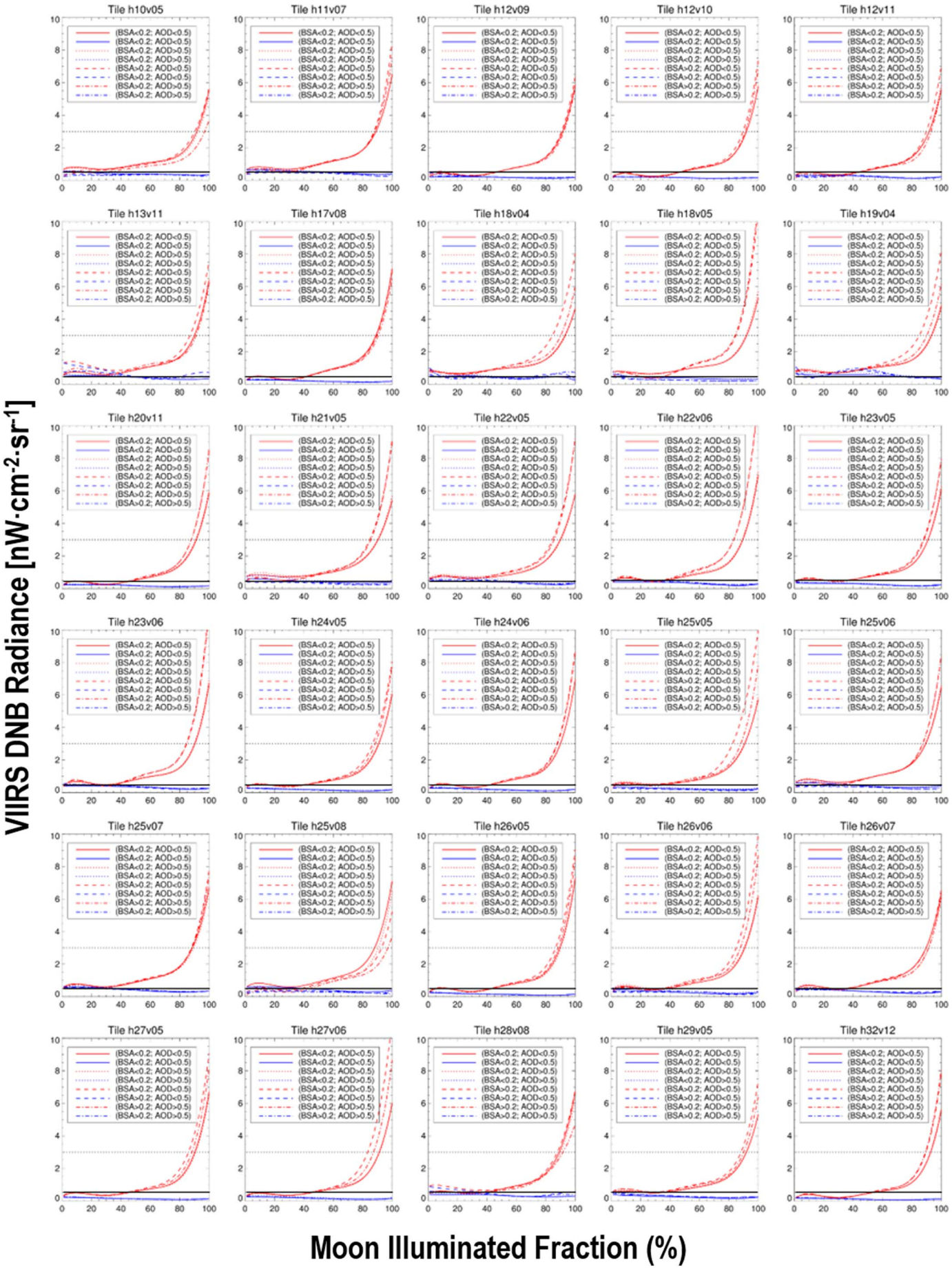

Fig. 11. Results for benchmark test #3: NTL (BSA, AOD). Set up is the same as Fig. 7.

effects in terms of light diffusion and even side-illumination can introduce spurious results.

Results point to a PCT of 89.03% under moonless conditions, 81.92% under moonlit conditions, and a global PCT of 85.5% under all conditions tested. Note that the PCT values reported in this test only describe the overall performance of the VCM vis-à-vis the NASA Black Marble NTL data processing chain. As such, results are not representative of the true performance characteristics of the nighttime VCM product. This is particularly the case since NTL artifacts (*e.g.*, Aurora and mid- to high-latitudes), while temporary in nature, can also set off the product's QA flags; thus, resulting in slightly lower VCM PCT values. Nevertheless, this benchmark test provides insights into potential areas for improvement in the VCM algorithm. In particular, the comparatively lower PCT values under moonlit conditions underscore the need for considering variations in surface brightness, as routinely done in daytime VCM processing.

4.3. Pixel-based variations in NTL

The increased utility of the VIIRS Day/Night Band sensor to capture sub-pixel NTL features, has led to a considerable number of studies that have utilized the underlying radiances directly at the pixel-level (Cao and Bai, 2014; Chen et al., 2015; Elvidge et al., 2015; Guo et al., 2015; Hu et al., 2015; Lee et al., 2014; Mann et al., 2016; Ou et al., 2015; Sharma et al., 2016; Shi et al., 2014; Straka et al., 2015; Zhao et al., 2016). The wide range of applications makes it therefore necessary to establish the sensitivity of residual errors and extraneous artifacts in the NTL retrievals through explicit assessment of product performance at

Table 3
Summary statistics for benchmark test #2 – NTL (VZA, BSA) – based on a discrete range of View Zenith Angles (VZA < 45°, VZA ≥ 45°) and Black-Sky Albedos (BSA < 0.2, BSA ≥ 0.2). Set up is the same as Table 2.

TILE ID	Minimum detectable radiance (L_{min})				Retrieval uncertainty @ L_{min} (L_0)			
	TOA	VNP46A2	TOA	VNP46A2	TOA	VNP46A2	TOA	VNP46A2
	Moon fraction < 50%		Moon fraction ≥ 50%		Moon fraction < 50%		Moon fraction ≥ 50%	
h10v05	0.645	0.406	2.373	0.326	0.089	0.045	1.360	0.029
h11v07	0.694	0.542	3.217	0.364	0.102	0.044	2.053	0.058
h12v09	0.378	0.243	2.520	0.154	0.085	0.033	1.747	0.015
h12v10	0.333	0.195	2.641	0.134	0.097	0.015	1.929	0.010
h12v11	0.391	0.267	2.538	0.164	0.085	0.027	1.761	0.034
h13v11	0.821	0.698	2.975	0.421	0.126	0.109	1.879	0.069
h17v08	0.419	0.267	2.948	0.160	0.100	0.032	2.010	0.018
h18v04	0.766	0.512	2.793	0.468	0.100	0.097	1.597	0.095
h18v05	0.661	0.417	3.512	0.278	0.116	0.084	2.394	0.014
h19v04	0.820	0.669	2.793	0.477	0.076	0.117	1.619	0.115
h20v11	0.356	0.232	2.958	0.135	0.085	0.019	2.196	0.018
h21v05	0.716	0.504	3.293	0.335	0.073	0.052	2.115	0.023
h22v05	0.720	0.531	3.326	0.321	0.068	0.025	2.198	0.049
h22v06	0.581	0.440	3.890	0.259	0.105	0.020	2.831	0.043
h23v05	0.545	0.339	2.963	0.200	0.076	0.028	2.071	0.031
h23v06	0.599	0.440	3.709	0.266	0.118	0.030	2.695	0.037
h24v05	0.462	0.236	2.983	0.137	0.068	0.036	2.143	0.024
h24v06	0.440	0.256	3.186	0.146	0.098	0.039	2.374	0.029
h25v05	0.542	0.307	3.231	0.188	0.065	0.040	2.237	0.019
h25v06	0.656	0.485	3.262	0.307	0.097	0.049	2.176	0.031
h25v07	0.697	0.552	3.166	0.337	0.089	0.054	2.038	0.032
h25v08	0.525	0.415	2.589	0.282	0.108	0.036	1.550	0.038
h26v05	0.442	0.215	3.222	0.118	0.095	0.041	2.415	0.022
h26v06	0.555	0.374	3.279	0.226	0.099	0.035	2.292	0.035
h26v07	0.573	0.437	2.786	0.272	0.098	0.052	1.793	0.030
h27v05	0.430	0.195	3.109	0.105	0.077	0.035	2.319	0.017
h27v06	0.429	0.242	3.290	0.125	0.076	0.037	2.428	0.020
h28v08	0.617	0.495	2.793	0.328	0.071	0.068	1.791	0.050
h29v05	0.617	0.370	2.746	0.221	0.070	0.063	1.749	0.021
h32v12	0.305	0.156	2.667	0.083	0.085	0.030	2.082	0.022

Table 4
Summary statistics for benchmark test #3 – NTL (BSA, AOD) – based on a discrete range of Black-Sky Albedos (BSA < 0.2, BSA ≥ 0.2) and Aerosol Optical Depths (AOD < 0.5, AOD ≥ 0.5). Set up is the same as Table 2.

TILE ID	Minimum detectable radiance (L_{min})				Retrieval uncertainty @ L_{min} (L_0)			
	TOA	VNP46A2	TOA	VNP46A2	TOA	VNP46A2	TOA	VNP46A2
	Moon fraction < 50%		Moon fraction ≥ 50%		Moon fraction < 50%		Moon fraction ≥ 50%	
h10v05	0.513	0.320	1.865	0.247	0.065	0.037	1.040	0.023
h11v07	0.684	0.532	3.059	0.387	0.114	0.048	1.934	0.058
h12v09	0.346	0.215	2.368	0.146	0.067	0.023	1.624	0.015
h12v10	0.313	0.175	2.480	0.127	0.085	0.012	1.791	0.009
h12v11	0.367	0.256	2.357	0.153	0.075	0.040	1.565	0.033
h13v11	0.819	0.691	2.753	0.415	0.107	0.117	1.694	0.078
h17v08	0.383	0.239	2.793	0.151	0.092	0.027	1.887	0.017
h18v04	0.678	0.484	2.646	0.382	0.082	0.116	1.590	0.091
h18v05	0.618	0.384	3.230	0.247	0.109	0.085	2.197	0.017
h19v04	0.738	0.549	2.715	0.393	0.076	0.080	1.661	0.075
h20v11	0.326	0.204	2.646	0.122	0.070	0.025	1.903	0.022
h21v05	0.638	0.422	3.009	0.276	0.064	0.048	1.942	0.023
h22v05	0.712	0.511	3.202	0.302	0.071	0.033	2.068	0.043
h22v06	0.618	0.451	3.997	0.286	0.099	0.023	2.879	0.039
h23v05	0.542	0.344	2.779	0.200	0.066	0.039	1.916	0.028
h23v06	0.604	0.454	3.593	0.281	0.121	0.029	2.575	0.045
h24v05	0.447	0.225	2.863	0.127	0.061	0.037	2.029	0.023
h24v06	0.431	0.255	2.986	0.146	0.090	0.041	2.197	0.029
h25v05	0.509	0.271	3.260	0.161	0.045	0.040	2.254	0.017
h25v06	0.631	0.466	3.065	0.291	0.083	0.057	2.014	0.024
h25v07	0.587	0.463	2.698	0.298	0.089	0.048	1.705	0.033
h25v08	0.467	0.372	2.047	0.252	0.091	0.044	1.281	0.036
h26v05	0.426	0.201	3.067	0.112	0.087	0.037	2.263	0.019
h26v06	0.519	0.337	3.150	0.204	0.091	0.040	2.181	0.033
h26v07	0.406	0.302	2.063	0.193	0.068	0.034	1.300	0.021
h27v05	0.419	0.187	3.073	0.099	0.070	0.033	2.282	0.016
h27v06	0.409	0.220	3.166	0.114	0.070	0.032	2.337	0.017
h28v08	0.531	0.409	2.537	0.284	0.064	0.054	1.673	0.044
h29v05	0.601	0.365	2.646	0.216	0.066	0.060	1.674	0.024
h32v12	0.289	0.143	2.484	0.076	0.080	0.028	1.916	0.021

the native pixel scale. Accordingly, we conducted a series of pixel-based benchmark tests to address the following three questions:

- Benchmark test #5: What is the fraction of the variation in the pixel-based NTL time series that can be explained by variations in moon-illuminated reflectance anisotropy (hereby termed the lunar BRDF effect)?
- Benchmark test #6: What is the fraction of the variation in the pixel-based NTL time series that can be explained by changes in snow cover?
- Benchmark test #7: What is the fraction of the variation in the pixel-based NTL time series that is explained by seasonal changes in canopy-level foliage?

The performance metrics for benchmark tests #5 and #6 are both expressed in terms of the square of Pearson coefficient ($R^2 \times 100\%$) between the 5-year NTL daily time series data and the periodicity of the lunar cycle (defined using daily values of moon-illumination fraction). To estimate the R^2, we fitted a 5th order polynomial between these two variables - *i.e.*, NTL(Moon Illuminated Fraction) – to establish the same relationships observed in Figs. 6–11 at the individual pixel-level.

For these three tests, we employed a random stratified sample of 72,000 individual TOA and VNP46A2 grid cells representing a diverse range of urban covers, surface conditions, and latitudinal gradients. As with benchmark tests #1 to #3, these tests were based on the entire available Collection V001 DNB time series record (2012–mid 2017), comprising the same sample Level-3 tiles listed in Tables 2–4. In order to establish realistic NTL detection limits relative to anticipated changes in NTL, we used the Global Urban Footprint product (Esch et al., 2013, 2017) to ensure that the stratified sample was also spatially

Table 5
Summary statistics for benchmark test #4 (VCM Performance Test). Values describe the total probability of correct typing (PCT) corresponding to each sample VIIRS Level 3 tile, as well as for six different groupings (as done in benchmark tests #1 to #3) based on a discrete range of BSA, VZA, and AOD values observed for moon illuminated fractions < 50%.

TILE ID	Total PCT	PCT by grouping (moon fraction < 50%)					
		VZA < 45°	VZA ≥ 45°	BSA < 0.2	BSA ≥ 0.2	AOD < 0.5	AOD ≥ 0.5
h10v05	90.46%	91.30%	89.01%	94.27%	67.27%	90.85%	88.65%
h11v07	92.66%	94.22%	91.00%	95.69%	69.37%	92.98%	91.82%
h12v09	92.62%	95.72%	89.37%	94.64%	74.81%	93.14%	91.02%
h12v10	92.96%	94.19%	91.59%	96.07%	71.10%	92.95%	92.99%
h12v11	91.62%	91.83%	91.35%	96.89%	62.01%	91.59%	91.81%
h13v11	93.62%	93.48%	93.78%	97.17%	70.21%	93.88%	92.32%
h17v08	93.15%	95.29%	90.92%	95.57%	72.54%	94.42%	91.30%
h18v04	82.26%	88.05%	69.71%	85.31%	71.55%	83.58%	72.15%
h18v05	87.17%	87.13%	87.25%	87.92%	87.02%	87.44%	86.67%
h19v04	80.86%	88.28%	66.12%	82.93%	72.94%	82.79%	68.63%
h20v11	79.90%	88.50%	70.65%	82.86%	71.53%	79.04%	83.19%
h21v05	83.64%	85.39%	81.26%	88.56%	80.00%	84.67%	81.15%
h22v05	86.43%	86.89%	85.69%	92.07%	83.33%	87.06%	85.16%
h22v06	86.91%	86.87%	86.96%	80.91%	87.54%	86.62%	87.38%
h23v05	85.63%	86.20%	84.72%	91.16%	82.21%	86.34%	84.18%
h23v06	85.70%	86.33%	84.91%	85.82%	85.67%	85.74%	85.63%
h24v05	86.00%	86.62%	84.99%	90.53%	83.73%	86.63%	84.53%
h24v06	85.85%	86.41%	85.10%	90.23%	82.00%	85.91%	85.76%
h25v05	89.09%	89.46%	88.51%	92.04%	86.06%	89.28%	88.46%
h25v06	90.55%	90.82%	90.21%	96.78%	78.38%	90.65%	90.42%
h25v07	92.54%	93.38%	91.62%	96.76%	66.31%	92.91%	91.93%
h25v08	94.65%	95.78%	93.47%	96.99%	77.40%	95.50%	92.59%
h26v05	89.36%	89.93%	88.45%	88.66%	89.63%	89.39%	89.26%
h26v06	91.08%	91.21%	90.91%	95.80%	70.67%	91.59%	90.32%
h26v07	91.67%	92.50%	90.73%	95.53%	62.05%	92.75%	89.97%
h27v05	90.26%	90.65%	89.65%	92.76%	88.23%	90.54%	89.25%
h27v06	92.84%	93.75%	91.69%	95.43%	77.05%	93.51%	90.60%
h28v08	94.48%	97.20%	91.72%	95.85%	83.87%	95.24%	91.62%
h29v05	89.69%	90.76%	88.01%	94.56%	66.68%	90.30%	88.30%
h32v12	87.32%	86.92%	87.97%	93.90%	57.94%	87.36%	87.06%

representative of different stages of urban growth – from sparse rural (% Urban = 0) to densely built-up pixels (% Urban = 100%).

Results for benchmark test #5 are illustrated in Fig. 12a. Note that, in the case of the TOA product, benchmark test #5 measures the degree of dependence in L_{DNB} (*cf.*, Eq. (1)) to Lunar BRDF effects (after cloud correction) for a wide range of percent urban covers.

Conversely, for the refined product (VNP46A2), this test measures the residual variance in L_{NTL} caused by lunar reflectance anisotropy effects after cloud-, atmospheric-, BRDF-, and seasonal (P_{gap}) correction. Results for the VNP46A2 product, therefore, demonstrate how the lunar BRDF effect can be reduced down to a Pearson R^2 coefficient of 0.37, across low-density urban pixels (and thus, low-intensity NTL), and even lower (< 0.10) for high-density urban pixels (and thus, high-intensity NTL). The VNP46A2 product enhancements, therefore, result in a substantial reduction of residual lunar contamination relative to the cloud-cleared TOA data, which had high R^2 values, ranging from [0.4, 0.9], for DNB pixels experiencing both low to high percent urban covers. The Lunar BRDF effect is further illustrated in Figs. 15–16; where the TOA time series exhibits large bumps and wiggles that trail the lunar cycle.

Results for benchmark test #6 illustrate the TOA and VNP46A2 products' performance as a function of observed variations in snow cover (Fig. 12b). The dependence of the pixel-based values to Lunar BRDF effects, resulting from moon-reflected snow surfaces, remained well < 0.30 (Pearson R^2 coefficient), a substantial enhancement relative to the cloud-cleared TOA data. Since the Lunar BRDF effect was measured as a function of the number of cloud-free snow-covered days within each DNB grid cell, benchmark test #6 can be used to assess the ability of the NASA Black Marble algorithm to effectively capture snow-covered surfaces. The comparatively lower R^2 values across VNP46A2 pixels with short snow days (< 10% of the S-NPP time series) demonstrate the VNP46A2 product's ability to correctly activate the current day snow status flag – a critical step for triggering the snow BRDF/albedo algorithm process necessary to mitigate downstream errors in the VNP46 product. This is particularly relevant for NTL conditions experiencing short but intense periods of snow cover, where highly

Table 6
Summary statistics for benchmark test #4 (VCM Performance Test) describe the total probability of correct typing (PCT) under moon illuminated fractions ≥50%. Setup is the same as Table 5.

TILE ID	Total PCT	PCT by grouping (moon fraction ≥ 50%)					
		VZA < 45°	VZA ≥ 45°	BSA < 0.2	BSA ≥ 0.2	AOD < 0.5	AOD ≥ 0.5
h10v05	84.77%	86.50%	81.79%	87.26%	68.86%	85.09%	83.23%
h11v07	82.06%	83.75%	80.23%	83.52%	71.17%	82.91%	79.84%
h12v09	86.83%	88.74%	84.90%	88.23%	72.55%	87.65%	84.49%
h12v10	85.99%	86.36%	85.59%	87.14%	77.57%	86.27%	84.94%
h12v11	88.76%	88.93%	88.55%	91.03%	74.63%	89.15%	86.66%
h13v11	88.17%	87.89%	88.53%	89.93%	74.51%	88.56%	86.38%
h17v08	87.70%	89.51%	85.85%	88.92%	76.23%	90.60%	83.55%
h18v04	79.38%	85.41%	66.37%	79.63%	78.58%	80.40%	70.96%
h18v05	75.68%	76.27%	74.78%	76.70%	75.50%	76.38%	74.37%
h19v04	77.97%	85.35%	62.87%	78.46%	76.18%	79.84%	65.17%
h20v11	74.69%	83.05%	65.54%	72.00%	82.14%	74.16%	76.62%
h21v05	76.44%	79.30%	72.56%	76.98%	76.10%	77.28%	74.32%
h22v05	78.79%	79.66%	77.37%	81.41%	77.69%	79.55%	77.19%
h22v06	71.92%	72.46%	71.24%	69.30%	72.16%	72.65%	70.73%
h23v05	79.71%	80.16%	78.99%	78.86%	80.09%	79.81%	79.49%
h23v06	71.90%	72.57%	71.08%	73.19%	71.56%	71.68%	72.32%
h24v05	80.22%	80.99%	78.94%	78.09%	80.97%	80.16%	80.37%
h24v06	77.88%	78.63%	76.88%	76.30%	78.96%	77.77%	78.04%
h25v05	82.40%	83.31%	80.91%	83.63%	81.34%	82.07%	83.55%
h25v06	81.95%	83.19%	80.39%	82.41%	81.22%	82.81%	80.86%
h25v07	83.58%	85.01%	82.02%	84.82%	76.21%	85.63%	80.36%
h25v08	86.40%	88.96%	83.76%	86.91%	82.59%	88.31%	82.39%
h26v05	82.11%	82.98%	80.75%	79.72%	82.76%	81.93%	82.96%
h26v06	82.74%	84.03%	81.12%	83.94%	77.77%	84.43%	80.14%
h26v07	84.30%	85.50%	82.96%	85.50%	73.18%	87.66%	79.46%
h27v05	82.47%	83.00%	81.61%	84.16%	81.41%	82.58%	82.04%
h27v06	85.45%	86.27%	84.42%	86.29%	79.72%	86.34%	82.45%
h28v08	90.59%	92.61%	88.55%	90.96%	87.12%	92.15%	84.73%
h29v05	83.75%	85.80%	80.51%	85.02%	78.30%	85.17%	80.24%
h32v12	82.89%	83.38%	82.09%	83.95%	79.19%	83.82%	76.30%

reflective snow can introduce large positive biases in the final NTL estimates (Bennett and Smith, 2017; Levin, 2017; Román and Stokes, 2015). It is also necessary for robust outlier detection; where the actual moon/aerosol/albedo contribution is needed to establish the boundary NTL conditions. This latter idea is demonstrated in Fig. 5, where extraneous light emissions caused by the Aurora Borealis north of Lake Superior were located over snow- and cloud-contaminated DNB pixels. This would have led to significant errors of cloud-, snow-, and aurora-leakage, which, due to the use of BRDF corrected pixels as a baseline, were correctly classified as outliers by the VNP46 algorithm. Such higher order effects, which are common at daily time scales, underscore the need to routinely retrieve daily DNB BRDF quantities to better account for these rapidly changing scenarios. In fact, we found that a standalone climatology, based on *a-priori* (annual or monthly) DNB BRDF values, while useful for helping mitigate data gaps in the daily BRDF time series, resulted in increased contamination from ephemeral snow and other changing conditions.

Results for benchmark test #7 illustrate how the seasonal increase in canopy-level foliage during the winter and summer months (as described in Section 2.3) does not affect the trend in the VNP46A2 NTL time series record. This refinement is illustrated in the sample plots shown in Fig. 13, where the pixel-level VNP46A2 values (blue points) do not predominate along the central region of the 2nd quadrant ($X \leq 0$; $Y \geq 0$, or the area inside the dotted black circles in Fig. 13), where increases in the magnitude of NTL during winter periods track corresponding increases in green foliage between summer and winter periods. The seasonal effect was found to be most pronounced across temperate regions (*e.g.*, US, European, and Asia tiles: h10v05; h18v04; h18v05; h24v05; h25v05; h26v05; h29v05) as confirmed by previous studies (Bennett and Smith, 2017; Levin, 2017; Levin and Zhang, 2017). We also found additional deviations across sample Level 3 tiles in West Africa (h17v08) and South Africa (h20v11); suggesting that seasonal variations in NTL are likely to be more pervasive than originally thought. Previous assessments had thus far examined the seasonal variations using spatially- and temporally-aggregated NTL products (*e.g.*, monthly moon-free composites at city-wide scales). The results

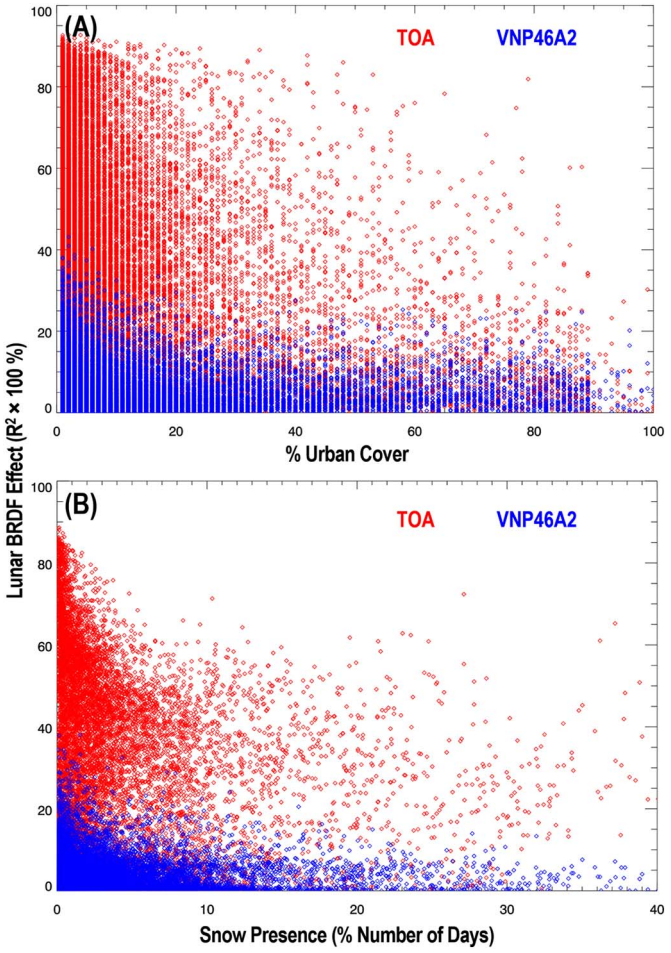

Fig. 12. The correlation between a 5-year time series of daily nighttime lights (NTL) and lunar phase for the cloud-corrected at-sensor DNB radiance product (TOA: shown in red) and NASA's Black Marble daily moonlight adjusted nighttime lights (NTL) product (VNP46A2: shown in blue) shown as a function of (A) percent urban cover (benchmark test #5) and (B) snow presence (benchmark test #6). (For interpretation of the references to colour in this figure legend, the reader is referred to the web version of this article.)

from benchmark test #7, however, provide additional new insights of the variations at finer spatial and temporal scales.

5. Validation efforts

The series of benchmark tests introduced in Section 4.1–4.3 were designed to quantify errors inherited from the upstream products (*i.e.*, VIIRS calibrated radiances, cloud mask, aerosol retrieval, *etc.*) These evaluations, however, only provide a relative assessment of NTL product performance. To establish the absolute accuracy of the final NTL retrievals, one must also assess the NTL products against an independent source of reference data. Unfortunately, quality-assessed *in-situ* NTL measurements are not widely available; let alone, at the spatial and temporal densities necessary to capture the full range of retrieval conditions. Recent NASA Black Marble product validation efforts have therefore focused on developing guidelines for accuracy assessment of NTL products through a number of international initiatives described in the following subsections.

5.1. GEO's nighttime product validation task

Under the Group on Earth Observations (GEO) Human Planet Initiative's 2017–2019 Work Programme, a Nighttime Product Validation (NPV) task was recently established to foster the development of advanced accuracy assessment of NTL time series products. A key deliverable of the NPV task is the development of a good practices protocol focusing on quantitative validation of satellite-derived NTL products. Key components to be included as part of this protocol, are: (1) variable definitions and accuracy metrics following traceable units of the Système Internationale (SI); (2) best practice guidelines for field sampling and scaling techniques; (3) recommendations for reporting and use of accurate information; (4) guidelines for product inter-comparison exercises; and (5) recommendations for data and information exchange.

5.2. Pitahaya field experiment

Under technical guidance from GEO Human Planet Initiative's NPV task, Puerto Rico's Working Group on Light Pollution (PRWGLP) seeks to develop measurement standards and protocols for *in-situ* data collection. The primary driver for this activity is the development of a sustainable development indicator, based on NTL time series data, to meet the multiple regulatory and scientific aspects of PR's light pollution laws and ordinances. To that end, a number of scoping exercises were recently conducted across multiple light pollution abatement zones in Puerto Rico. This included a successful deployment of a stable point source at the Pitahaya Farmland site in Cabo Rojo, PR (Fig. 14).

During the night of 2 March 2017, at 2:00 local time, the PRWGLP team conducted a validation experiment at the aforementioned Pitahaya site. A stable point source was reflected by a 30 m^2 Lambertian target to generate an in-band DNB radiance at sensor (L_{DNB}) of ~0.45nW·cm^{-2}·sr^{-1}. Additional Sky-Quality Meter (SQM) data recordings (Falchi et al., 2016; Kyba et al., 2011, 2013; Schnitt et al., 2013) with specialized filters matching the VIIRS relative spectral response (RSR), as well as atmospheric measurements from nearby AERONET sun photometers (Holben et al., 1998) were used to characterize atmospheric conditions.

The validation approach follows the assessment method first described in *Cao and Bai* (2014), which relies on quantitative analysis and stability monitoring of stable light point sources. We used the following parameters to generate our radiative transfer calculations: (1) atmospheric transmittance = 0.8 (based on 6S radiative transfer code and AERONET calculations), a target reflectance = 0.8, and 16 W of total effective irradiance incident on the reflective surface. Results in Fig. 14 also illustrate how the detected VIIRS at-sensor cloud-corrected radiance (TOA) and VNP46A2 estimates over the pixel centered on the reflective point source were within the VNP46A2 product's "Breakthrough" requirement for L_{min} (0.43 nW·cm^{-2}·sr^{-1}) – after removing background noise measured the days prior and after activation of the stable light point sources. We found that the final VNP46A2 product resulted in a 16.95% sensitivity enhancement (due to improved reduction background noise), as confirmed in previous benchmark tests, compared to the at-sensor cloud-corrected radiance product (TOA) under observed moon-free conditions.

6. Temporal patterns of nighttime lights dynamics

This section provides a number of examples representing different temporal patterns of NTL dynamics. The following sections provide a description for each time series archetype and their corresponding areas of interest.

6.1. Rapid urbanization

Fig. 15a shows the expansion of road networks and light industrial units across the Jebel Ali Free Zone (Jafza) in Dubai, United Arab Emirates (UAE). The free zone contributes 21% of Dubai's GDP on a yearly basis and it sustains the employment of > 144,000 people. > 7000 global companies are based in Jafza; helping account for almost 32% of total foreign direct investment flow into the UAE.

Note that the VNP46A2 time series (blue curve) achieves the lowest

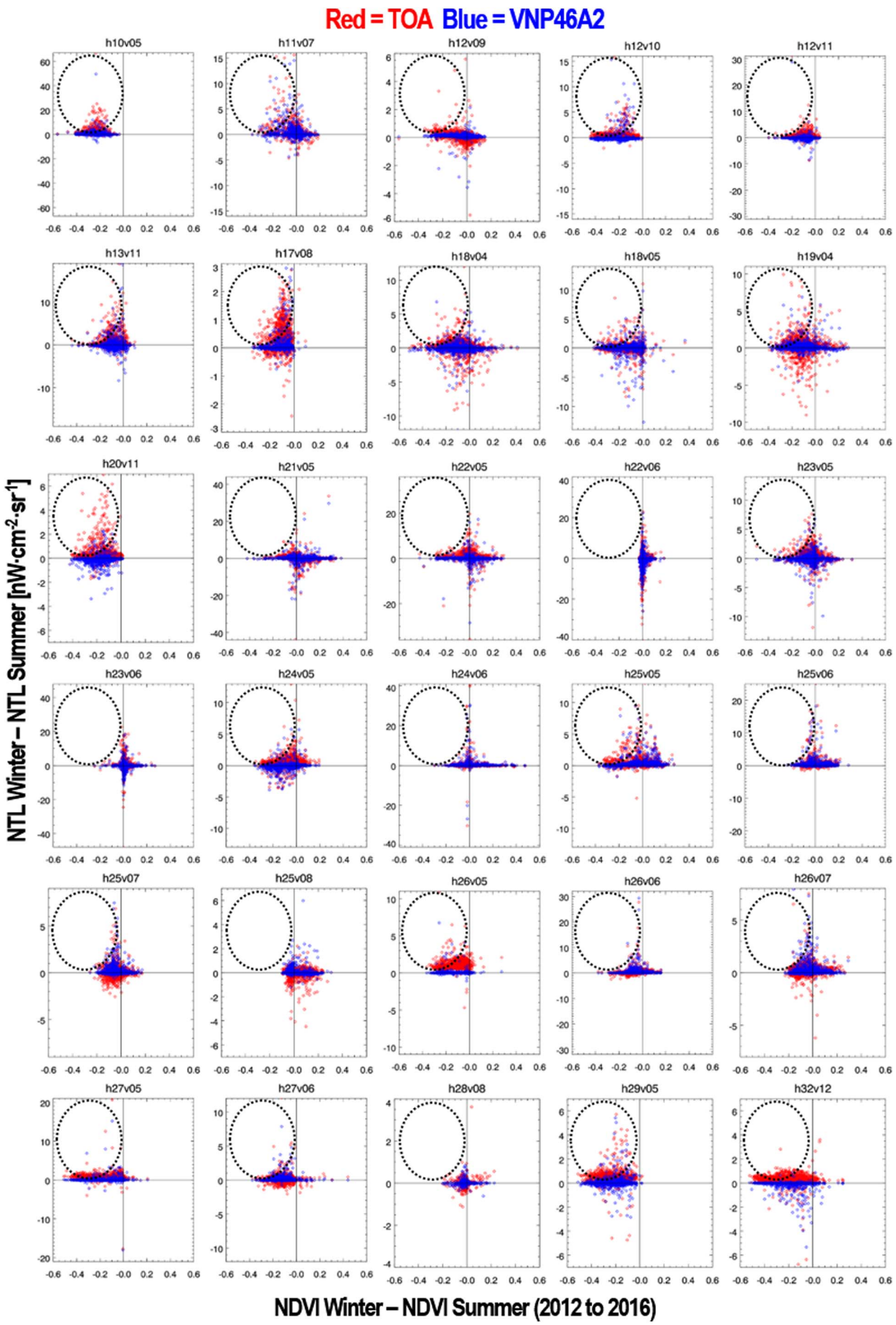

(caption on next page)

Fig. 13. Results for benchmark test #7. The effects of seasonal variations of NTL with NDVI between winter and summer periods (*i.e.*, pixels within black-dotted circles in upper-left quadrants) are shown for 30 sample Level 3 tiles for the cloud-corrected at-sensor DNB radiance product (TOA: shown in red), and NASA's Black Marble daily moonlight adjusted nighttime lights (NTL) product (VNP46A2: shown in blue). (For interpretation of the references to colour in this figure legend, the reader is referred to the web version of this article.)

noise levels for all NTL archetypes presented in Section 6. This can be attributed to a number of factors tied to improved product performance. For example, across low-lit NTL areas exhibiting rapid land-cover and land use changes (LCLUC), or where the initial NTL conditions are close to 0 $nW{\cdot}cm^{-2}{\cdot}sr^{-1}$ (*e.g.*, Fig. 16c and d), we found that a reduction in Lunar BRDF artifacts (shown in the TOA products as consistent bumps and wiggles that trail the lunar cycle) leads to a re-adjustment of the linear trend in NTL. Thus, by improving the temporal representation of initial NTL conditions, the VNP46A2 product is particularly suited for the study of urbanization pathways (Seto and Dhakal, 2014) at these high frequency daily time intervals.

We also note that the relative large temporal daily radiance variations observed across cases is often the result of the spatial observation coverage mismatch among days due to the difference of the DNB view geometry (*i.e.*, a 740 m footprint moving outside a 500 m gridded area). As a result, the radiance may vary significantly within a smaller spatial coverage; particularly close to city center. Additional testing indicated that the temporal variation can be significantly reduced by applying a 3 by 3-pixel averaging window to the VNP46 time series data. However, this would result in a coarser spatial resolution. Ultimately, the choice to account for these temporal variations depends on the specific application (pixel-based or otherwise) to determine whether such a process is needed.

6.2. Socioeconomic patterns and cultural factors

Fig. 15 illustrates three additional NTL archetypes. Fig. 15b shows a parcel near Mount Arafat near Mecca. Saudi Arabia. This barren area exhibits an oscillatory seasonal cycle in NTL. The latter is postulated to be related to the activities surrounding the Hajj Pilgrimage, where NTL have been observed to change dramatically as prayer and eating during the Holiday shifts later into the night (Román and Stokes, 2015). Fig. 15c shows the NTL time series profile for a village in Korhogo, Ivory Coast. The area of interest exhibited gradual increases in NTL during a 4-year period, beginning in 2013. Upon investigation, it was found that in 2012, the city of Korhogo received financial support from international banks and aid organizations to improve access to basic infrastructure, including renewable electricity (World Bank, 2017). Fig. 15d shows the NTL time series profile for a village in Shenmu, a county-level city in the north of Shaanxi province, China. The highly coal-dependent city, one of China's top economic producers, experienced a sudden production decline in 2013 due to the coal market's downturn. This resulted in a deep recession with thousands of businesses closing. Moreover, the excessive coal mining over the years has led to serious damage to the local ecological environment. The sharp peaks observed in 2016 and 2017 are the result of short-term periods of snow cover.

6.3. Conflict-affected displaced populations

Fig. 16 illustrates the tracking of NTL-related patterns that describe the conditions of conflicted affected populations across Syria and neighboring Jordan. Fig. 16a shows the NTL time series profile for a residential district in Damascus; a city which suffered significant damage to its infrastructure during the early stages of the Syrian civil war. Fig. 16b shows the NTL time series for a rural area in the town of Jarabulus, Syria. In 2016, the population of Jarabulus swelled to 25,000 citizens from 3500, weeks after the Turkey-backed Free Syrian Army liberated the northern Syrian town in Aleppo province. This abrupt demographic upward shift was captured by the VNP46A2 product, where the NTL time series profile reached a maximum of 2 $nW{\cdot}cm^{-2}{\cdot}sr^{-1}$ (below the JPSS L_{min} threshold requirement) or 65% of

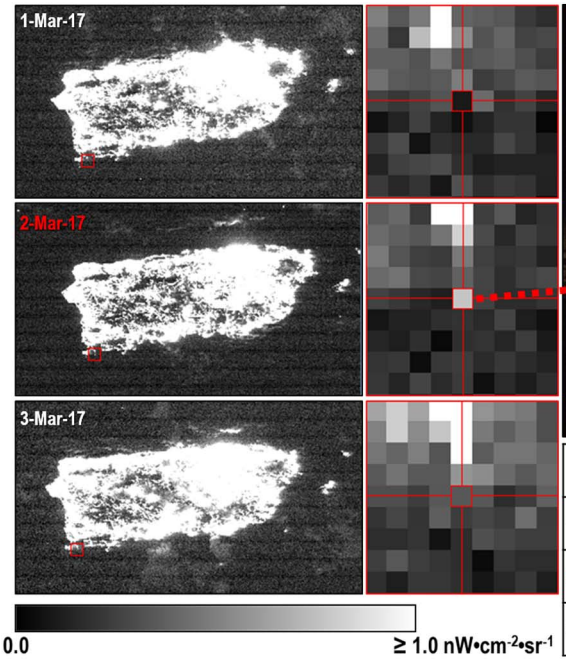

DATE	TOA	VNP46A2	VCM	VZA	AOD	BSA	LZA
1-Mar-17	1.04	2.15	0	27.90°	0.180	0.104	158.25°
2-Mar-17	7.65	6.22	0	8.520°	0.210	0.090	145.26°
3-Mar-17	3.41	1.62	0	40.54°	0.108	0.104	129.64°

Fig. 14. The NTL radiances at the Pitahaya Farmland site in Cabo Rojo, PR on 1st, 2nd and 3rd March 2017. The top-right image shows the setup of the stable point source. TOA and VNP46A2 values are in $nW{\cdot}cm^{-2}{\cdot}sr^{-1}$. VCM = 0 represents cloud free overpasses. LZA is lunar zenith angle, and the values larger than 108° correspond to moonless nights.

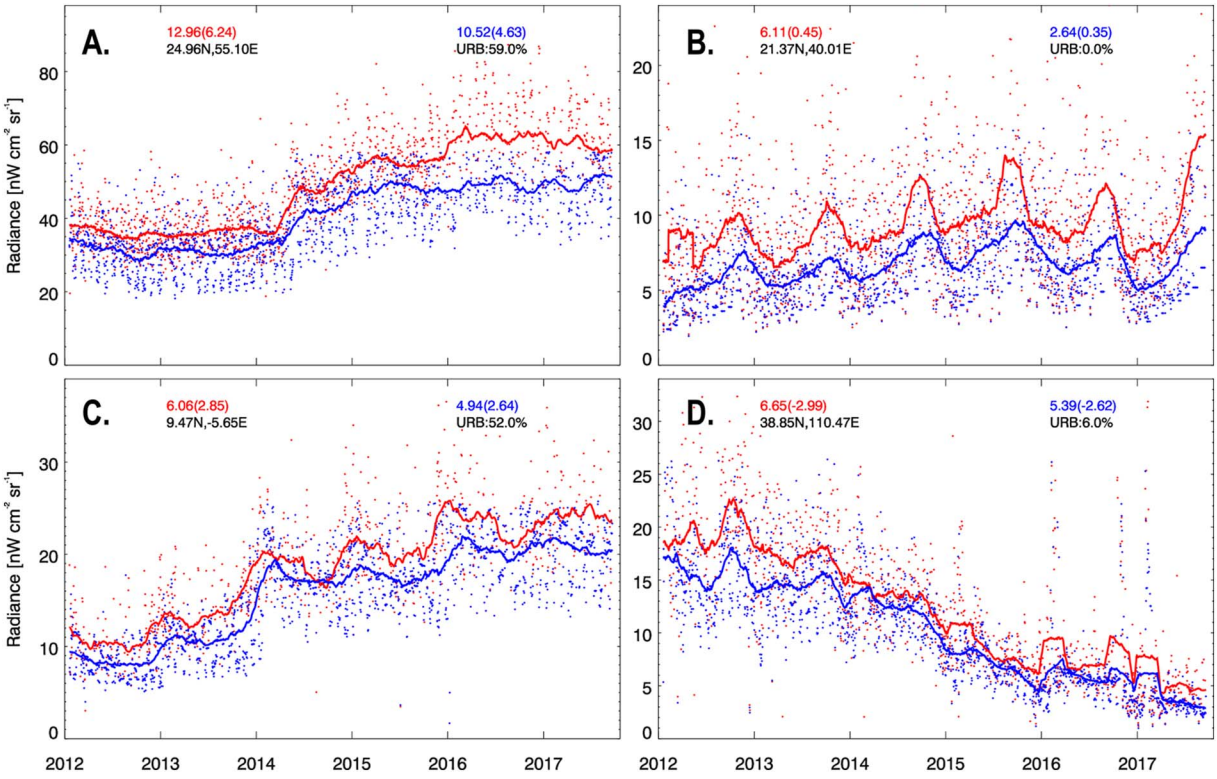

Fig. 15. Five-year time series plots illustrate the types of changes that can be inferred from NASA's Black Marble product suite. In addition to abrupt short-term changes caused by (A) rapid urban growth and (C) electrification, the VNP46 product can detect cyclical changes driven by reoccurring human activities *e.g.*, (B) the Ramadan holiday period, as well as (D) gradual changes caused by regional economic changes and out-migration. The original at-sensor cloud-corrected DNB radiances (TOA) (in units of $nW{\cdot}cm^{-2}{\cdot}sr^{-1}$) are shown as red points. Those resulting from NASA's Lunar BRDF Adjusted NTL product (VNP46A2) are shown as blue points. The trailing solid red and blue curves correspond to the daily-rolling average (using a 90-day moving window). The numbers on the top panels illustrate the anticipated noise reduction (σ^2) for each method. The numbers in parenthesis refer to the estimated linear trend in NTL per year. The numbers on the bottom panels show the center point's coordinates (Latitude, Longitude). URB is the % Urban cover as reported by the Global Urban Footprint product. (For interpretation of the references to colour in this figure legend, the reader is referred to the web version of this article.)

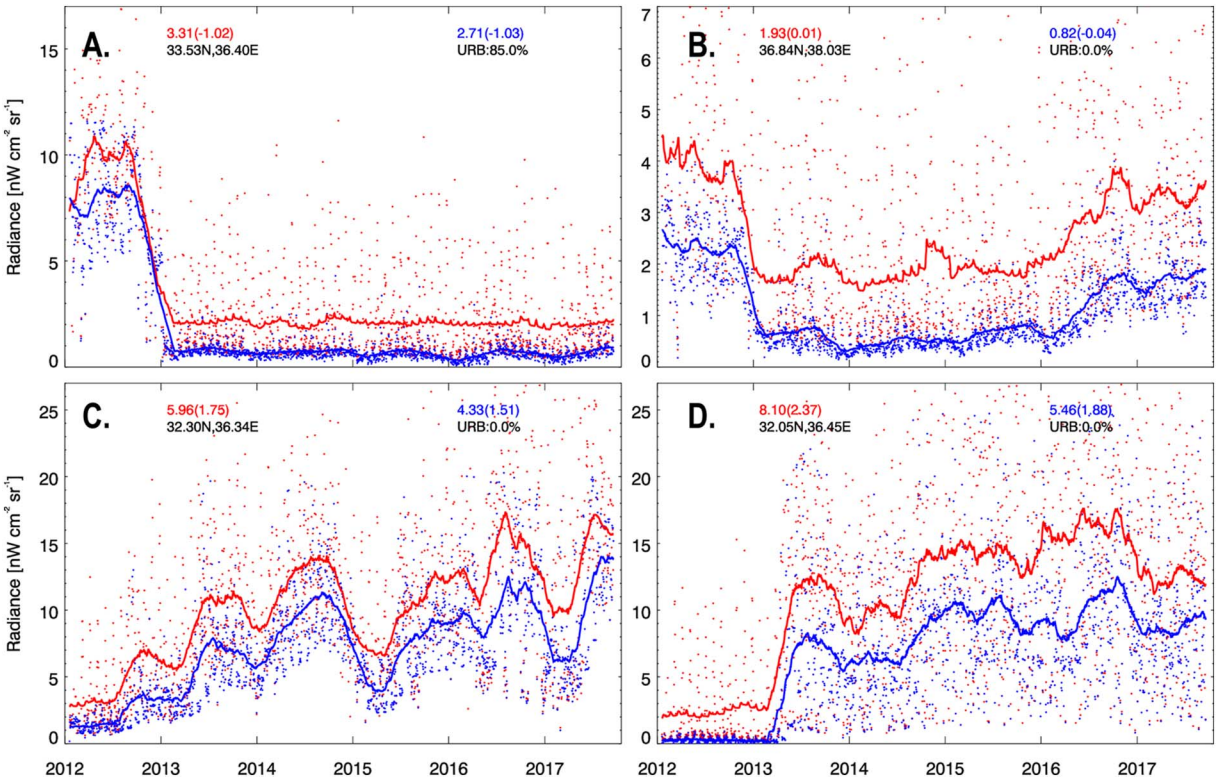

Fig. 16. Five-year time series plots across four different locations illustrate the tracking of abrupt NTL-related changes that describe conditions of conflicted affected populations in Syria. Setup is the same as Fig. 15.

the pre-event NTL conditions. Fig. 16c shows how the Black Marble NTL time series data can also trace the ensuing movement of Syrian citizens across the Jordanian border into the Zaatari refugee camp. Since July 2012, Zaatari has been transformed from a barren desert village with a population of 12,000, into a three-square-mile tent city where over 140,000 Syrian refugees are estimated to dwell. To date, Zaatari is Jordan's fourth-largest population center and the world's second largest refugee camp (Helios Global, 2017). We posit that the large variations observed in the Zaatari camp (between 2014 and 2017) are largely due to refugee movements, seasonal migrations, and weather changes. Rain in particular makes conditions challenging as refugees prepare for the cold winter. Workers in the camp often have to clear flooded areas near shelters, to ease the movement of refugees and allow services to access the beneficiaries (NRC, 2017). Due to the maximum capacity of 60,000 refugees in Zaatari, a second camp was built in March 2013. The Mrajeeb Al Fhood (Emirati) refugee camp (shown in Fig. 15d) is located across a stretch of arid plains some 20 km east of Zarqa, Jordan. It was opened in April 2013 and is funded by the UAE. The camp was built to cope with the influx of more Syrian refugees, as the capacity of the Zaatari refugee camp was showing to be insufficient. As of 18 September 2017, the camp has a population of 7243 refugees (UNHCR, 2017).

6.4. Changes to the VIIRS DNB's relative spectral response (RSR)

Of importance to note, the VIIRS DNB on Suomi-NPP cannot reliably capture the technological transition of street lighting from conventional (*e.g.*, incandescent or high-pressure sodium lamps) to light emitting diodes (LED). As confirmed in previous studies, the VIIRS DNB's RSR does not include the blue-light emission peak of the White LEDs (Cao and Bai, 2014; Falchi et al., 2016).

Studies have pointed how a blue-shift of the VIIRS DNB RSR, to capture the primary LED emission peak between 450 and 460 nm, and secondary peak near 550 nm, would enable superior monitoring of changes related to LEDs (Elvidge et al., 2010). On the other hand, a blue-shift to the RSR will result in greater atmospheric contamination from molecular scatter, which must be adjusted for in the NASA Black Marble products. Such a shift may also enable other practical uses related to the detection of bioluminescence, whose relatively narrow band of principal emission fall outside of the current DNB response function. Miller et al. (2005, 2006) present one example of bioluminescent detection from the previous-generation DMSP/OLS sensors, whose RSR is blue-shifted by ~100 nm with respect to the DNB. It was calculated that the bioluminescent signal would need to be nearly twice as strong to be detected by DNB technology, due to the RSR shift, despite the DNB being significantly improved in terms of spatial resolution, radiometric resolution, and signal-to-noise specifications.

While the improvement to LED characterization and potential for enabling the detection of bioluminescence are appealing outcomes of an RSR blue-shift, other applications related to nightglow sensitivity (*e.g.*, Miller et al., 2012a, 2012b) may suffer. These include new insights to middle-atmospheric dynamics, made possible by the DNB's sensitivity to hydroxyl emissions in the near-infrared (Miller et al., 2015). These same nightglow emissions present a source of noise to NASA Black Marble products (another benefit to the RSR blue-shift from the perspective of NTL applications). This is all to say that, with any consideration for future day/night band additions or modifications, trade studies tied to individual product performance, overarching mission goals and priorities, constraints on sensor design, bandwidth, and costs, must all be counterbalanced. A positive step in this regard is the recent 2017–2027 Decadal Survey Report on Earth Science and Applications from Space (NASM, 2018), whose Weather and Air Quality Panel highlighted the importance of developing "A higher-resolution VIIRS-like instrument (200 m horizontal resolution) with the day-night band and an update frequency of 3 hours". Note this specification currently drives the 'Goal' requirement for the NASA's Black Marble product suite (Table 1).

7. Conclusions

With a quickly expanding temporal record of well-calibrated global nocturnal imagery, the Day/Night Band (DNB) sensor of the Visible Infrared Imaging Radiometer Suite (VIIRS) is starting to emerge from its early exploratory stage to become a new global baseline for nighttime remote sensing data. When properly accounting for systematic sources of retrieval uncertainty and measurement error, NASA's Black Marble product suite (VNP46) enables the use of the VIIRS DNB for global mapping of nighttime lights (NTL) as related to human-driven patterns and processes. These processes include seasonal changes driven by recurring human activities, gradual changes due to electrification and economic conditions, as well as abrupt short-term changes caused by disturbances in power delivery, such as disasters and conflict. In addition to these temporal patterns, studies related to an assortment of other processes (*e.g.*, changes in lighting associated with different social and economic sectors) can benefit from a daily long-term NTL record to establish how urbanization processes differ both within and across cities.

We describe the unique features of the VNP46 algorithm, including routine correction for Lunar BRDF, cloud, terrain, atmospheric, snow, airglow, stray light, and seasonal effects. These refinements, along with intelligent gap-filling protocols, enable the first-ever daily monitoring of low-lit NTL structures, with a substantial sensitivity enhancement (of a factor of 7) compared to the current specification established by the Joint Polar Satellite System (JPSS). Owing to a rigorous quality control process, results over a global sample of 30 Level 3 tiles indicate that the standard NASA Black Marble product (VNP46A2) maintains a near constant background radiance profile across the entire lunar illumination cycle, well within the "Breakthrough" and "Goal" performance requirements for detection limit (L_{min}) and robustness (L_0). The resulting performance enhancements were also confirmed through time series analyses of archetypes from different temporal patterns of urbanization dynamics, including displaced settlements and low-NTL areas of concentrated energy poverty.

As a validation exercise, we evaluated NASA's Black Marble daily moonlight adjusted NTL product (VNP46A2) against a stable point source at the Pitahaya Farmland site in Cabo Rojo, Puerto Rico. A daily change of 0.43 $nW{\cdot}cm^{-2}{\cdot}sr^{-1}$ was successfully detected, helping establish the reasonableness of summary statistics for L_{min} (0.29 $nW{\cdot}cm^{-2}{\cdot}sr^{-1}$) and L_0 (0.04 $nW{\cdot}cm^{-2}{\cdot}sr^{-1}$) extracted from extensive benchmark tests. At the pixel-level, the dependence of VNP46A2 NTL time series data to Lunar BRDF effects was also reduced by 60% (down to an R^2 coefficient under 0.37) across low-density urban areas, and by 30% (down to an R^2 coefficient under 0.10) across high density urban areas.

Accurate estimation of daily surface reflectance anisotropy (BRDF) and albedo information, retrieved from daytime multi-angular DNB surface reflectance observations, were shown to be essential processing steps for the removal of extraneous sources of NTL emissions in the VNP46A2 product. This was especially true for urban areas located across desert and semi-arid regions, as well as other scenarios experiencing high surface albedos > 0.2 (*e.g.*, snow-covered areas). Under these situations, we found that the daily NTL patterns, based on cloud-corrected at-sensor (TOA) data alone, were exposed to higher-order aerosol coupling effects which, in the absence of proper Lunar BRDF and atmospheric correction, severely impacted retrieval quality.

The overall performance of the VIIRS nighttime cloud mask was

found to be comparable to the JPSS specification. The overall PCT was 89.03% under moonless conditions, 81.92% under moonlit conditions, and 85.5% for all conditions tested. These results are consistent with early assessments of the VCM product (*e.g.*, Kopp et al. (2014) reported a global PCT for land areas at night of 86.4%). The performance of the VCM was also found to worsen under nighttime conditions with high albedos. This suggests that explicit specification of surface conditions in the VCM is key to reduce instances of cloud leakage. Considering that the VIIRS DNB was originally designed to detect nighttime clouds, efforts to adapt the DNB data in the VCM process should be explored as a means to improve performance. Additional consideration of Lunar BRDF effects in the downstream NTL retrieval process also helps reduce cloud leakage effects, particularly under snow, desert, and semi-arid surfaces.

Another major source of uncertainty in the NTL time series data – snow cover impacts – was reduced through the activation of the VIIRS daily snow status flags and snow albedo values. As a result, the fraction of the variation in the pixel-based NTL time series that can be explained by detected changes in snow cover, was reduced by 65% (down to an R2 coefficient under 0.30). Based on these results, to capture other rapid seasonal variations, particularly across spatially heterogeneous conditions (*e.g.*, flooded surfaces, agricultural-urban and forest-urban mosaics), we recommend that both a daily snow-free and a daily snow BRDF/albedo retrieval be implemented in place of a monthly or annual climatology (Moody et al., 2008; Román et al., 2011, 2013; Strugnell et al., 2001; Wang et al., 2012). Recent studies have found that these *a-priori* BRDF archetypes can result in a poor-quality BRDF/albedo, and thus a poor-quality NTL, retrieval; due to the climatology's failure to resolve high frequency surface changes (Liu et al., 2017, 2017; Moustafa et al., 2017; Schaaf et al., 2011; Wang et al., 2012, 2014, 2018).

We also found that temporal aggregation of at-sensor NTL radiances, in lieu of proper daily atmospheric and BRDF correction, resulted in comparatively smaller (and thus worse) noise reduction levels relative to the daily VNP46A2 product. These findings help dispel various assumptions surrounding the quality of VIIRS NTL time series data, namely that: (1) VIIRS NTL time series products can only be produced reliably from nearest-nadir observations under moonless nights; and (2) that at-sensor TOA data under moonless nights are, by default, less prone to sources of uncertainty and measurement error. Results from our seven series of global benchmark tests, combined with further examinations of a representative sample of NTL time series typologies (Figs. 15–16), show the opposite effect to be true – *i.e.*, that at-sensor TOA VIIRS DNB data under moonless nights are in fact more subjected to sources of uncertainty and measurement error, resulting in higher noise levels. As reported in previous studies, there are several higher order artifacts that persist in the VIIRS DNB time series under moonless conditions, including: (1) a seasonal tendency of “false clear” and “false cloud” detections in the current (V001) VIIRS Cloud Mask, (2) residual striping and stray light artifacts that remain after on-orbit calibration, (3) the influence of nightglow, and (4) the short-lived presence of aurora or solar glare events at mid- to high-latitudes (Cao et al., 2013; Cao and Bai, 2014; Lee et al., 2015; Miller et al., 2013; Mills and Miller, 2016).

We introduced and assessed the performance of a vegetation dispersion parameter, generally known as the clumping index, to parameterize the confined distribution of foliage within distinct canopy structures. The adoption of pixel-based canopy gap probability (P_{gap}) measures in the VNP46 algorithm helps address an unresolved source of measurement uncertainty in the VIIRS NTL time series (Levin, 2017; Levin and Zhang, 2017). Note that accurate assessment and removal of seasonal variations in NTL is not only critical for time series change detection, but also essential for understanding how green space design mediates ecological functioning and thus ecosystem services in the urban environment (Andersson et al., 2014; Heynen et al., 2006; Jim, 2004; Wolch et al., 2014). For instance, cities like Barcelona (O'Sullivan, 2017), Berlin (Kabisch and Haase, 2014), and Bangkok (Thaiutsa et al., 2008), are embarking upon major plans to raise their proportion of urban green zones to reduce urban heat island effects, air pollution, and other environmental issues. A 30% increase in green zones, *e.g.*, is equivalent to adding ~3–10 m^2 of green area per city resident.

The influence of atmospheric effects on NTL continues to be a dominant source of retrieval uncertainty; particularly at daily time scales, and over cities in developing countries – where levels of air pollution (and thus atmospheric turbidity) have increased significantly in the past decades (Tomasi et al., 2017). Multiple nighttime AOD retrieval strategies were examined as part of the NASA Black Marble algorithm development effort; including daytime-to-daytime averaged AOD values *vs*. direct estimation over temporally stable NTL pixels (Johnson et al., 2013). The current (Collection V001) algorithm implementation uses the “daytime-to-daytime averaged” approach and preliminary results are shown to be promising. However, given the relatively nascent nature of nighttime AOD retrievals using the DNB, new approaches are still being considered.

We should also note that nighttime lights emitted from within urban areas can exhibit a strong BRDF phenomenon, mainly due to the 3D-dimensional physiognomy and structure of buildings in cities. However, the correction of this effect is challenging due to a lack of empirical data and radiative transfer models. Continued research and experimental work will be crucial to discover and better understand these processes.

Key to achieving the goals as set out by the Group on Earth Observations (GEO) Human Planet Initiative's Nighttime Product Validation (NPV) task is the enhanced assessment of nighttime aerosol and P_{gap} estimates. To support these evaluations, our future validation plan calls for the synergistic use of high-quality airborne (Cook et al., 2013) and terrestrial LiDAR data (Paynter et al., 2016), combined with high resolution daytime and nighttime satellite imagery. These activities will help provide more direct estimates of canopy gap fraction in urban environments; helping establish more realistic constraints in the P_{gap} retrieval process. Likewise, we anticipate that available nighttime aerosol measurements (*e.g.*, from AERONET, Cloud-Aerosol Lidar with Orthogonal Polarization (CALIOP), and Cloud-Aerosol Transport System (CATS) retrievals) (Omar et al., 2013; Yorks et al., 2015, 2016) will be used to support future NTL product validation efforts. Efforts are also underway to deploy additional nightlight point sources, with improved small target radiometry and standards-traceable understanding. The long-term goal is to establish NTL reference sites at different locations covering a wide range of land, atmospheric, and illumination conditions.

Potential science users advised of the provisional nature of the current VNP46 product suite (Collection V001) bearing in mind factors such as: (1) upcoming refinements to the VIIRS DNB calibration software and ancillary data sources, (2) residual striping and stray light artifacts that remain after on-orbit calibration, and (3) the performance of the VIIRS nighttime cloud mask. We anticipate that these caveats will be mitigated in the upcoming (Collection V002) reprocessing of the VIIRS long-term archive; making the products increasingly more valuable for global Earth System science and near-real time applications.

Acknowledgements

The authors would like to thank Dr. George Riggs (GSFC/SSAI) for his support in reviewing this manuscript. The authors gratefully acknowledge support provided by NASA's Office of the Chief Scientist

under the Science Innovation Fund (SIF), as well as NASA's Earth Science Data and Information Systems (EOSDIS), Terra/Aqua/Suomi-NPP, and Applied Sciences Programs under NASA Grants #NNX16D11G, #80NSSC17K0172, NNH16ZDA001N-16-GEO16-0055, and NNH17ZDA001N-TASNPP17-0007. We also thank the Office of Naval Research (ONR) Multidisciplinary University Research Initiative (MURI) program through contract N00014-16-1-2040 (Grant 11843919).

Appendix A. Data Format

NASA's Black Marble data are provided in the standard land HDF-EOS (Hierarchical Data Format - Earth Observing System) format. The filenames follow a naming convention which gives useful information regarding the specific product. For example, the filename VNP46A1.A2015001.h08v05.001.2017012234657.hdf indicates:

- VNP46A1 - Product Short Name
- .A2015001 - Julian Date of Acquisition (A-YYYYDDD)
- .h08v05 - Tile Identifier (horizontalXXverticalYY)
- 0.001 - Collection Version
- .2017012234657- Julian Date of Production (YYYYDDDHHMMSS)
- .hdf - Data Format (HDF-EOS)
- Format (HDF-EOS)

Table A1
Scientific data sets included in the VNP46A1 product.

Scientific data sets (HDF Layers)	Units	Bit type	Fill value	Valid range
DNB_At_Sensor_Radiance_500m	$nW{\cdot}cm^{-2}{\cdot}sr^{-1}$	16-Bit unsigned integer	65,535	0–65,534
Sensor_Zenith	Degrees	16-Bit signed integer	−32,768	−90–90
Sensor_Azimuth	Degrees	16-Bit signed integer	−32,768	−180–180
Solar_Zenith	Degrees	16-Bit signed integer	−32,768	0–180
Solar_Azimuth	Degrees	16-Bit signed integer	−32,768	−180–180
Lunar_Zenith	Degrees	16-Bit signed integer	−32,768	0–180
Lunar_Azimuth	Degrees	16-Bit signed integer	−32,768	−180–180
Glint_Angle	Degrees	16-Bit signed integer	−32,768	−180–180
UTC_Time	Decimal Hours	32-Bit floating point	−999.9	0–24
QF_Cloud_Mask	Class flag	16-Bit unsigned integer	65,535	0–65,534
QF_DNB	Class flag	8-Bit unsigned integer	255	0–254
Radiance_M10	$W{\cdot}m^{-2}{\cdot}\mu m^{-1}{\cdot}sr^{-1}$	16-Bit unsigned integer	65,535	0–65,534
Radiance_M11	$W{\cdot}m^{-2}{\cdot}\mu m^{-1}{\cdot}sr^{-1}$	16-Bit unsigned integer	65,535	0–65,534
BrightnessTemperature_M12	Kelvins	16-Bit unsigned integer	65,535	0–65,534
BrightnessTemperature_M13	Kelvins	16-Bit unsigned integer	65,535	0–65,534
BrightnessTemperature_M15	Kelvins	16-Bit unsigned integer	65,535	0–65,534
BrightnessTemperature_M16	Kelvins	16-Bit unsigned integer	65,535	0–65,534
QF_VIIRS_M10	Class flag	8-Bit unsigned integer	255	0–254
QF_VIIRS_M11	Class flag	8-Bit unsigned integer	255	0–254
QF_VIIRS_M12	Class flag	8-Bit unsigned integer	255	0–254
QF_VIIRS_M13	Class flag	8-Bit unsigned integer	255	0–254
QF_VIIRS_M15	Class flag	8-Bit unsigned integer	255	0–254
QF_VIIRS_M16	Class flag	8-Bit unsigned integer	255	0–254
Moon_Phase_Angle	Degrees	16-Bit signed integer	−32,768	0–180
Moon_Illumination_Fraction	Degrees	16-Bit signed integer	−32,768	0–100
Granule	None	8-Bit unsigned integer,	255	0–254

Table A2
Scientific data sets included in the VNP46A2 product.

Scientific data sets (HDF layers)	Units	Bit type	Fill value	Valid range
DNB_BRDF-Corrected_NTL_500m	$nWatts{\cdot}cm^{-2}{\cdot}sr^{-1}$	16-Bit unsigned integer	65,535	0–65,534
Mandatory_Quality_Flag	Class flag	8-Bit unsigned integer	255	0–3
Latest_High_Quality_Retrieval	Number of Days	8-Bit unsigned integer	255	0–254
Snow_Flag	Class flag	8-Bit unsigned integer	255	0–1
QF_Cloud_Mask	Class flag	16-Bit unsigned integer	65,535	0–65,534

Appendix B. QA metadata

Details of flag description key and quality flags of the product VNP46A1 and VNP46A2 are shown in following tables.

Table A3
Values of QF_Cloud_Mask in the VNP46A1 product.

Bit	Flag description key	Results
0	Day/night	0 = Night 1 = Day
1–3	Land/water background	000 = Land & Desert 001 = Land no Desert 010 = Inland Water 011 = Sea Water 101 = Coastal
4–5	Cloud mask quality	00 = Poor 01 = Low 10 = Medium 11 = High
6–7	Cloud detection results & confidence indicator	00 = Confident Clear 01 = Probably Clear 10 = Probably Cloudy 11 = Confident Cloudy
8	Shadow detected	1 = Yes 0 = No
9	Cirrus detection (IR) (BTM15-BTM16)	1 = Cloud 0 = No Cloud
10	Snow/ice surface	1 = snow/ice 0 = no snow/ice

Table A4
Values of the Mandatory_Quality_Flag in the VNP46A2 product.

Value	Retrieval quality	Algorithm instance
00	High-quality	Main algorithm (persistent nighttime lights)
01	Good-quality	Back up algorithm (temporal gap-filling)
02	Poor-quality	Back up algorithm (outlier removal)
255	No retrieval	Fill Value

Appendix C. Data archives

The VNP46 suite of products will be archived and supported by these data centers:
LAADS DAAC https://ladsweb.modaps.eosdis.nasa.gov/.
LANCE: NASA Near Real-time Data and Imagery https://earthdata.nasa.gov/earth-observation-data/near-real-time

Appendix D. Linear Lat/Lon Projection

NASA's Black Marble product suite (VNP46) employs the standard VIIRS Land science algorithms and software that produce the DNB standard (radiance-based) products, and their corresponding ancillary layers in gridded (Level 2G, Level 3) linear Lat/Lon format (Fig. 17). The gridding algorithms were modified to work with the VIIRS Day/Night Band's (DNB) unique viewing geometry, which, unlike the VIIRS moderate and imagery bands, has a ground pixel footprint at a nearly constant size (742 m). The rationale behind the VIIRS DNB gridding approach is to select the nighttime observations from available 6-min swath granules (2366 km along track, ~3100 km across-track), that are the least affected by cloud cover and off-nadir viewing observations. The goal is to increase signal-to-noise, while maximizing coverage within a cell of the gridded projection (Tan et al., 2006; Wolfe et al., 2002). By implementing this combined gridding strategy and geographic Linear Lat/Lon (LLL) projection formats, we seek to improve the efficiency of processing and reprocessing of the VNP46 product suite, preserve the satellite location and observation footprints, while also enabling the ingest of the products into accessible software for GIS-friendly analysis and mapping.

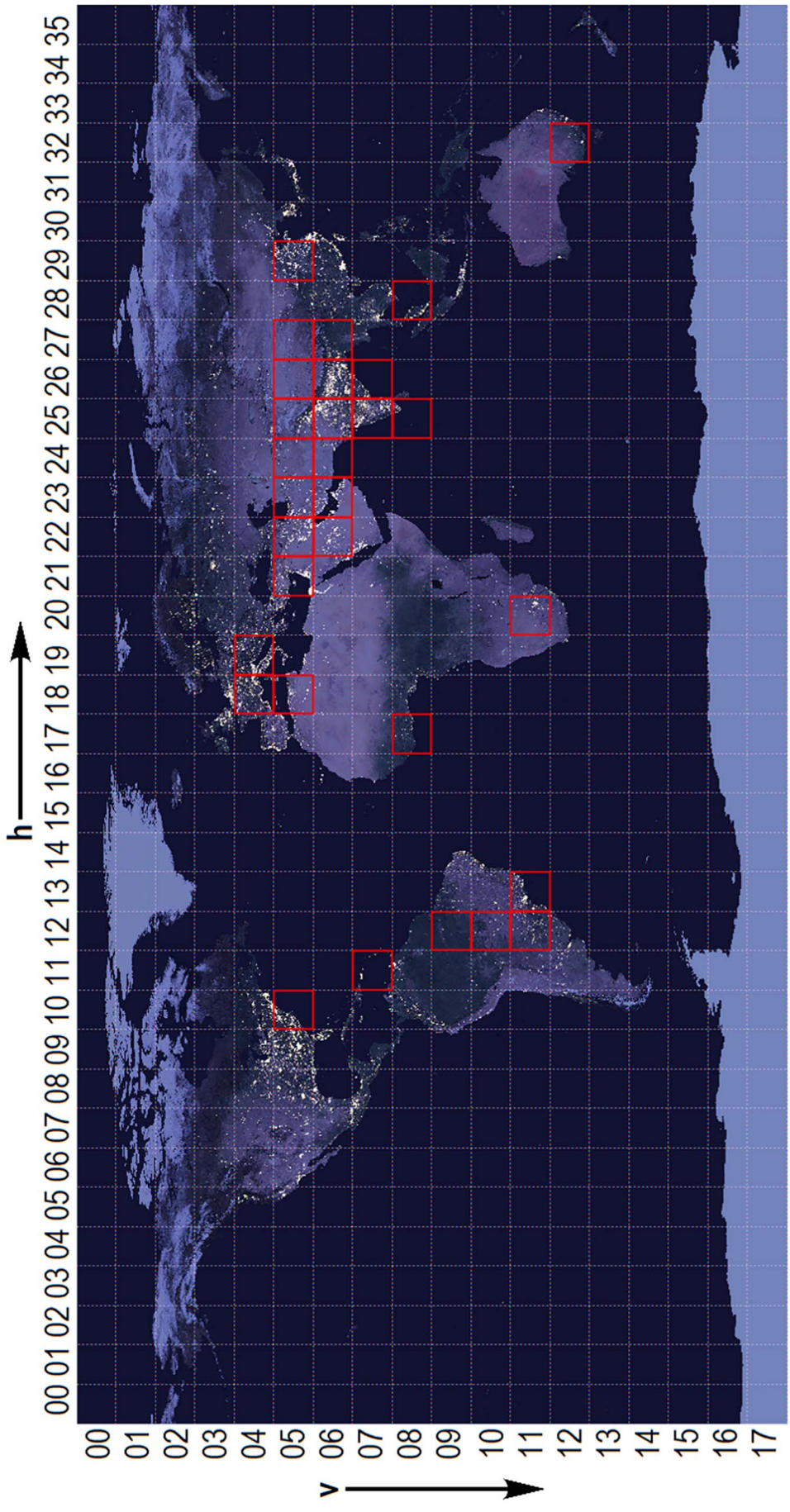

Fig. 17. The Suomi-NPP VIIRS linear latitude/longitude (or geographic) grid consists of 460 non-overlapping Land tiles which measure approximately $10^{\circ} \times 10^{\circ}$ region. 30 VIIRS tiles (highlighted in red) were used to conduct the benchmark tests presented in Section 4. (For interpretation of the references to colour in this figure legend, the reader is referred to the web version of this article.)

References

Andersson, E., Barthel, S., Borgström, S., Colding, J., Elmqvist, T., Folke, C., Gren, Å., 2014. Reconnecting cities to the biosphere: stewardship of green infrastructure and urban ecosystem services. Ambio 43, 445–453.

Asanuma, I., Yamaguchi, T., Park, J., Mackin, K.J., Mittleman, J., 2016. Detection limit of fishing boats by the day night band (DNB) on VIIRS. In: SPIE Optical Engineering + Applications. International Society for Optics and Photonics (p. 99760P–99760P–8).

Bankert, R.L., Solbrig, J.E., Lee, T.F., Miller, S.D., 2011. Automated lightning flash detection in nighttime visible satellite data. Weather Forecast. 26, 399–408.

Bennett, M.M., Smith, L.C., 2017. Advances in using multitemporal night-time lights satellite imagery to detect, estimate, and monitor socioeconomic dynamics. Remote Sens. Environ. 192, 176–197. http://dx.doi.org/10.1016/j.rse.2017.01.005.

Bennie, J., Davies, T.W., Inger, R., Gaston, K.J., 2014. Mapping artificial lightscapes for ecological studies. Methods Ecol. Evol. 5, 534–540. http://dx.doi.org/10.1111/2041-210X.12182.

Bickenbach, F., Bode, E., Nunnenkamp, P., Söder, M., 2016. Night lights and regional GDP. Rev. World Econ. 152, 425–447. http://dx.doi.org/10.1007/s10290-016-0246-0.

Campagnolo, M.L., Sun, Q., Liu, Y., Schaaf, C., Wang, Z., Román, M.O., 2016. Estimating the effective spatial resolution of the operational BRDF, albedo, and nadir reflectance products from MODIS and VIIRS. Remote Sens. Environ. 175, 52–64.

Cao, C., Bai, Y., 2014. Quantitative analysis of VIIRS DNB nightlight point source for light power estimation and stability monitoring. Remote Sens. 6, 11915–11935. http://dx.doi.org/10.3390/rs61211915.

Cao, C., Shao, X., Uprety, S., 2013. Detecting light outages after severe storms using the S-NPP/VIIRS day/night band radiances. IEEE Geosci. Remote Sens. Lett. 10, 1582–1586. http://dx.doi.org/10.1109/LGRS.2013.2262258.

Cescatti, A., Marcolla, B., Vannan, S.K.S., Pan, J.Y., Román, M.O., Yang, X., Ciais, P., Cook, R.B., Law, B.E., Matteucci, G., Migliavacca, M., Moors, E., Richardson, A.D., Seufert, G.G., Schaaf, C.B., 2012. Intercomparison of MODIS albedo retrievals and in situ measurements across the global FLUXNET network. Remote Sens. Environ. 121, 323–334. http://dx.doi.org/10.1016/j.rse.2012.02.019.

Chen, H., Xiong, X., Sun, C., Chen, X., Chiang, K., 2017. Suomi-NPP VIIRS day–night band on-orbit calibration and performance. J. Appl. Remote. Sens. 11, 36019.

Chen, J.M., Black, T.A., 1991. Measuring leaf area index of plant canopies with branch architecture. Agric. For. Meteorol. 57, 1–12.

Chen, J.M., Menges, C.H., Leblanc, S.G., 2005. Global mapping of foliage clumping index using multi-angular satellite data. Remote Sens. Environ. 97, 447–457. http://dx.doi.org/10.1016/j.rse.2005.05.003.

Chen, X., Nordhaus, W., 2015. A test of the new VIIRS lights data set: population and economic output in Africa. Remote Sens. 7, 4937–4947. http://dx.doi.org/10.3390/rs70404937.

Chen, Z., Yu, B., Hu, Y., Huang, C., Shi, K., Wu, J., 2015. Estimating house vacancy rate in metropolitan areas using NPP-VIIRS nighttime light composite data. IEEE J. Sel. Top. Appl. Earth Obs. Remote Sens. 8, 2188–2197. http://dx.doi.org/10.1109/JSTARS.2015.2418201.

Chopping, M.J., 2006. Progress in retrieving canopy structure parameters from NASA multi-angle remote sensing. In: International, I. (Ed.), Proceedings of the IEEE International Geoscience & Remote Sensing Symposium, IGARSS '06 and the 27th Canadian Remote Sensing Symposium. Denver, COpp. 256–259.

Cinzano, P., Falchi, F., Elvidge, C.D., Baugh, K.E., 2000. The artificial night sky brightness mapped from DMSP satellite operational linescan system measurements. Mon. Not. R. Astron. Soc. 318, 641–657.

Cole, T.A., Wanik, D.W., Molthan, A.L., Román, M.O., Griffin, R.E., 2017. Synergistic use of nighttime satellite data, electric utility infrastructure, and ambient population to improve power outage detections in urban areas. Remote Sens. 9, 286. http://dx.doi.org/10.3390/rs9030286.

Cook, B.D., Corp, L.A., Nelson, R.F., Middleton, E.M., Morton, D.C., McCorkel, J.T., Masek, J.G., Ranson, K.J., Ly, V., Montesano, P.M., 2013. NASA goddard's LiDAR, hyperspectral and thermal (G-LiHT) airborne imager. Remote Sens. 5, 4045–4066. http://dx.doi.org/10.3390/rs5084045.

Coscieme, L., Pulselli, F.M., Bastianoni, S., Elvidge, C.D., Anderson, S., Sutton, P.C., 2014. A thermodynamic geography: night-time satellite imagery as a proxy measure of emergy. Ambio 43, 969–979. http://dx.doi.org/10.1007/s13280-013-0468-5.

Elvidge, C.D., Keith, D.M., Tuttle, B.T., Baugh, K.E., 2010. Spectral identification of lighting type and character. Sensors 10, 3961–3988.

Elvidge, C.D., Zhizhin, M., Baugh, K., Hsu, F.-C., 2015. Automatic boat identification system for VIIRS low light imaging data. Remote Sens. 7, 3020–3036.

Elvidge, C.D., Zhizhin, M., Baugh, K., Hsu, F.-C., Ghosh, T., 2015. Methods for global survey of natural gas flaring from visible infrared imaging radiometer suite data. Energies 9, 14.

Esch, T., Heldens, W., Hirne, A., Keil, M., Marconcini, M., Roth, A., Zeidler, J., Dech, S., Strano, E., 2017. Breaking New Ground in Mapping Human Settlements From Space. The Global Urban Footprint (arXiv Prepr. arXiv1706.04862).

Esch, T., Marconcini, M., Felbier, A., Roth, A., Heldens, W., Huber, M., Schwinger, M., Taubenbock, H., Muller, A., Dech, S., 2013. Urban footprint processor-fully automated processing chain generating settlement masks from global data of the TanDEM-X mission. IEEE Geosci. Remote Sens. Lett. 10, 1617–1621. http://dx.doi.org/10.1109/LGRS.2013.2272953.

Falchi, F., Cinzano, P., Duriscoe, D., Kyba, C.C.M., Elvidge, C.D., Baugh, K., Portnov, B.A., Rybnikova, N.A., Furgoni, R., 2016. The new world atlas of artificial night sky brightness. Sci. Adv. 2, e1600377.

Gao, F., Morisette, J.T., Wolfe, R.E., Ederer, G., Pedelty, J., Masuoka, E., Myneni, R., Tan, B., Nightingale, J., 2008. An algorithm to produce temporally and spatially continuous MODIS LAI time series. IEEE Geosci. Remote Sens. Lett. 5, 60–64. http://dx.doi.org/10.1109/LGRS.2007.907971.

Griggs, D., Stafford-smith, M., Gaffney, O., Rockström, J., Öhman, M.C., Steffen, W., Glaser, G., Kanie, N., Noble, I., 2015. Policy: sustainable development goals for people and planet. Nature 495, 5–9. http://dx.doi.org/10.1038/495305a.

Guo, W., Lu, D., Wu, Y., Zhang, J., 2015. Mapping impervious surface distribution with integration of SNNP VIIRS-DNB and MODIS NDVI data. Remote Sens. 7, 12459–12477. http://dx.doi.org/10.3390/rs70912459.

He, L., Chen, J.M., Pisek, J., Schaaf, C.B., Strahler, A.H., 2012. Global clumping index map derived from the MODIS BRDF product. Remote Sens. Environ. 119, 118–130.

Helios Global, 2017. Helios Global World Trends [WWW Document]. URL. http://www.heliosglobalinc.com/world-trends-watch/ (accessed 10.24.17).

Heynen, N., Perkins, H.A., Roy, P., 2006. The political ecology of uneven urban green space: the impact of political economy on race and ethnicity in producing environmental inequality in Milwaukee. Urban Aff. Rev. 42, 3–25.

Hill, M.J., Román, M.O., Schaaf, C.B., 2011. Dynamics of vegetation indices in tropical and subtropical savannas defined by ecoregions and moderate resolution imaging spectroradiometer (MODIS) land cover. Geocarto Int. 1–39. http://dx.doi.org/10.1080/10106049.2011.626529.

Hillger, D., Kopp, T., Lee, T., Lindsey, D., Seaman, C., Miller, S., Solbrig, J., Kidder, S., Bachmeier, S., Jasmin, T., 2013. First-light imagery from Suomi NPP VIIRS. Bull. Am. Meteorol. Soc. 94, 1019–1029.

Holben, B.N., Eck, T.F., Slutsker, I., Tanré, D., Buis, J.P., Setzer, A., Vermote, E., Reagan, J.A., Kaufman, Y.J., Nakajima, T., Lavenu, F., Jankowiak, I., Smirnov, A., 1998. AERONET–a federated instrument network and data archive for aerosol characterization. Remote Sens. Environ. 66, 1–16. http://dx.doi.org/10.1016/S0034-4257(98)00031-5.

Hu, C., Chen, S., Wang, M., Murch, B., Taylor, J., 2015. Detecting surface oil slicks using VIIRS nighttime imagery under moon glint: a case study in the Gulf of Mexico. Remote Sens. Lett. 6, 295–301.

Huang, Q., Yang, X., Gao, B., Yang, Y., Zhao, Y., 2014. Application of DMSP/OLS nighttime light images: a meta-analysis and a systematic literature review. Remote Sens. 6, 6844–6866. http://dx.doi.org/10.3390/rs6086844.

Jiao, Z., Dong, Y., Schaaf, C.B., Chen, J.M., Román, M., Wang, Z., Zhang, H., Ding, A., Erb, A., Hill, M.J., Zhang, X., Strahler, A., 2018. An algorithm for the retrieval of the clumping index (CI) from the MODIS BRDF product using an adjusted version of the kernel-driven BRDF model. Remote Sens. Environ. http://dx.doi.org/10.1016/j.rse.2018.02.041.

Jiao, Z., Schaaf, C.B., Dong, Y., Román, M., Hill, M.J., Chen, J.M., Wang, Z., Zhang, H., Saenz, E., Poudyal, R., 2016. A method for improving hotspot directional signatures in BRDF models used for MODIS. Remote Sens. Environ. 186, 135–151.

Jim, C.Y., 2004. Green-space preservation and allocation for sustainable greening of compact cities. Cities 21, 311–320.

Johnson, R.S., Zhang, J., Hyer, E.J., Miller, S.D., Reid, J.S., 2013. Preliminary investigations toward nighttime aerosol optical depth retrievals from the VIIRS day/night band. Atmos. Meas. Tech. 6, 587–612.

Jönsson, P., Eklundh, L., 2002. Seasonality extraction by function fitting to time-series of satellite sensor data. IEEE Trans. Geosci. Remote Sens. 40, 1824–1832.

Jönsson, P., Eklundh, L., 2004. TIMESAT—a program for analyzing time-series of satellite sensor data. Comput. Geosci. 30, 833–845.

Kabisch, N., Haase, D., 2014. Green justice or just green? Provision of urban green spaces in Berlin, Germany. Landsc. Urban Plan. 122, 129–139.

Katz, Y., Levin, N., 2016. Quantifying urban light pollution - a comparison between field measurements and EROS-B imagery. Remote Sens. Environ. 177, 65–77. http://dx.doi.org/10.1016/j.rse.2016.02.017.

Klein, A.G., Stroeve, J., 2002. Development and validation of a snow albedo algorithm for the MODIS instrument. Ann. Glaciol. 34, 45–52.

Knyazikhin, Y., Glassy, J., Privette, J.L., Tian, Y., Lotsch, A., Zhang, Y., Wang, Y., Morisette, J.T., Votava, P., Myneni, R.B., Nemani, R.R., Running, S.W., 1999. MODIS Leaf Area Index (LAI) and Fraction of Photosynthetically Active Radiation Absorbed by Vegetation (FPAR) Product (MOD15) Algorithm Theoretical Basis Document. http://eospso.gsfc.nasa.gov/atbd/modistables.html.

Kopp, T.J., Thomas, W., Heidinger, A.K., Botambekov, D., Frey, R.A., Hutchison, K.D., Iisager, B.D., Brueske, K., Reed, B., 2014. The VIIRS cloud mask: progress in the first year of S-NPP toward a common cloud detection scheme. J. Geophys. Res. Atmos. 119, 2441–2456.

Kyba, C.C.M., Ruhtz, T., Fischer, J., Hölker, F., 2011. Cloud coverage acts as an amplifier for ecological light pollution in urban ecosystems. PLoS One 6, e17307.

Kyba, C.C.M., Wagner, J.M., Kuechly, H.U., Walker, C.E., Elvidge, C.D., Falchi, F., Ruhtz, T., Fischer, J., Hölker, F., 2013. Citizen science provides valuable data for monitoring global night sky luminance. Sci. Rep. 3 (1835). http://dx.doi.org/10.1038/srep01835.

Lacaze, R., Chen, J.M., Roujean, J.-L., Leblanc, S.G., 2002. Retrieval of vegetation clumping index using hot spot signatures measured by POLDER instrument. Remote Sens. Environ. 79, 84–95. http://dx.doi.org/10.1016/S0034-4257(01)00241-3.

Leblanc, S.G., Chen, J.M., White, H.P., Latifovic, R., Lacaze, R., Roujean, J.-L., 2005. Canada-wide foliage clumping index mapping from multiangular POLDER measurements. Can. J. Remote Sens. 31, 364–376.

Lee, S., Chiang, K., Xiong, X., Sun, C., Anderson, S., 2014. The S-NPP VIIRS day-night band on-orbit calibration/characterization and current state of SDR products. Remote Sens. 6, 12427–12446.

Lee, S., McIntire, J., Oudrari, H., Schwarting, T., Xiong, X., 2015. A new method for Suomi-NPP VIIRS day–night band on-orbit radiometric calibration. IEEE Trans. Geosci. Remote Sens. 53, 324–334. http://dx.doi.org/10.1109/TGRS.2014.2321835.

Levin, N., 2017. The impact of seasonal changes on observed nighttime brightness from

2014 to 2015 monthly VIIRS DNB composites. Remote Sens. Environ. 193, 150–164. http://dx.doi.org/10.1016/j.rse.2017.03.003.
Levin, N., Zhang, Q., 2017. A global analysis of factors controlling VIIRS nighttime light levels from densely populated areas. Remote Sens. Environ. 190, 366–382. http://dx.doi.org/10.1016/j.rse.2017.01.006.
Li, X., Strahler, A.H., 1992. Geometric-optical bidirectional reflectance modeling of the discrete crown vegetation canopy: Effect of crown shape and mutual shadowing. IEEE Trans. Geosci. Remote Sens. 30 (2), 276–292. http://dx.doi.org/10.1109/36.134078.
Li, X., Xu, H., Chen, X., Li, C., 2013. Potential of NPP-VIIRS nighttime light imagery for modeling the regional economy of China. Remote Sens. 5, 3057–3081. http://dx.doi.org/10.3390/rs5063057.
Liao, L.B., Weiss, S., Mills, S., Hauss, B., 2013. Suomi NPP VIIRS day-night band on-orbit performance. J. Geophys. Res. Atmos. 118, 12705–12718. http://dx.doi.org/10.1002/2013JD020475.
Liu, Y., Hu, C., Zhan, W., Sun, C., Murch, B., Ma, L., 2017. Identifying industrial heat sources using time-series of the VIIRS Nightfire product with an object-oriented approach. Remote Sens. Environ. http://dx.doi.org/10.1016/J.RSE.2017.10.019.
Liu, Y., Wang, Z., Sun, Q., Erb, A.M., Li, Z., Schaaf, C.B., Zhang, X., Román, M.O., Scott, R.L., Zhang, Q., 2017. Evaluation of the VIIRS BRDF, Albedo and NBAR products suite and an assessment of continuity with the long term MODIS record. Remote Sens. Environ. 201, 256–274.
Lucht, W., Roujean, J., 2000. Considerations in the parametric modeling of BRDF and albedo from multiangular satellite sensor observations. Remote Sens. Rev. 18, 343–379.
Ma, T., Zhou, C.H., Pei, T., Haynie, S., Fan, J.F., 2014. Responses of Suomi-NPP VIIRS-derived nighttime lights to socioeconomic activity in China's cities. Remote Sens. Lett. 5, 165–174. http://dx.doi.org/10.1080/2150704x.2014.890758.
Mann, M.L., Melaas, E.K., Malik, A., 2016. Using VIIRS day/night band to measure electricity supply reliability: preliminary results from Maharashtra, India. Remote Sens. 8, 711.
McHardy, T.M., Zhang, J., Reid, J.S., Miller, S.D., Hyer, E.J., Kuehn, R.E., 2015. An improved method for retrieving nighttime aerosol optical thickness from the VIIRS day/night band. Atmos. Meas. Tech. 8, 4773–4783.
Miller, Mills, S.P., Elvidge, C.D., Lindsey, D.T., Lee, T.F., Hawkins, J.D., 2012a. Suomi satellite brings to light a unique frontier of nighttime environmental sensing capabilities. Proc. Natl. Acad. Sci. 109, 15706–15711. http://dx.doi.org/10.1073/pnas.1207034109.
Miller, S.D., Combs, C.L., Kidder, S.Q., Lee, T.F., 2012b. Assessing moonlight availability for nighttime environmental applications by low-light visible polar-orbiting satellite sensors. J. Atmos. Ocean. Technol. 29, 538–557. http://dx.doi.org/10.1175/JTECH-D-11-00192.1.
Miller, S.D., Haddock, S.H.D., Elvidge, C.D., Lee, T.F., 2005. Detection of a bioluminescent milky sea from space. PNAS 102, 14181–14184. http://dx.doi.org/10.1073/pnas.0507253102.
Miller, S.D., Haddock, S.H.D., Elvidge, C.D., Lee, T.F., 2006. Twenty thousand leagues over the seas: the first satellite perspective on bioluminescent “milky seas.”. Int. J. Remote Sens. 27, 5131–5143. http://dx.doi.org/10.1080/01431160600554298.
Miller, S.D., Straka, W., Mills, S.P., Elvidge, C.D., Lee, T.F., Solbrig, J., Walther, A., Heidinger, A.K., Weiss, S.C., 2013. Illuminating the capabilities of the suomi national polar-orbiting partnership (NPP) visible infrared imaging radiometer suite (VIIRS) day/night band. Remote Sens. 5, 6717–6766.
Miller, S.D., Straka, W.C., Yue, J., Smith, S.M., Alexander, M.J., Hoffmann, L., Setvák, M., Partain, P.T., 2015. Upper atmospheric gravity wave details revealed in nightglow satellite imagery. Proc. Natl. Acad. Sci. 112, E6728–E6735.
Miller, S.D., Turner, R.E., 2009. A dynamic lunar spectral irradiance data set for NPOESS/VIIRS day/night band nighttime environmental applications. IEEE Trans. Geosci. Remote Sens. 47, 2316–2329. http://dx.doi.org/10.1109/TGRS.2009.2012696.
Mills, S., Miller, S., 2016. VIIRS day/night band—correcting striping and nonuniformity over a very large dynamic range. J. Imaging 2, 9. http://dx.doi.org/10.3390/jimaging2010009.
Mills, S., Weiss, S., Liang, C., 2013. VIIRS day/night band (DNB) stray light characterization and correction. In: SPIE Optical Engineering + Applications. International Society for Optics and Photonics, pp. 88661P.
Minnis, P., Hong, G., Sun-Mack, S., Smith, W.L., Chen, Y., Miller, S.D., 2016. Estimating nocturnal opaque ice cloud optical depth from MODIS multispectral infrared radiances using a neural network method. J. Geophys. Res. Atmos. 121, 4907–4932. http://dx.doi.org/10.1002/2015JD024456.
Molthan, A., Jedlovec, G., 2013. Satellite observations monitor outages from superstorm Sandy. Eos. Trans. Am. Geophys. Union 94, 53–54.
Moody, E.G., King, M.D., Schaaf, C.B., Platnick, S., 2008. MODIS-derived spatially complete surface albedo products: spatial and temporal pixel distribution and zonal averages. J. Appl. Meteorol. Climatol. 47, 2879–2894. http://dx.doi.org/10.1175/2008JAMC1795.1.
Moorthi, S., Pan, H.-L., Caplan, P., 2001. Changes to the 2001 NCEP Operational MRF/AVN Global Analysis/Forecast System. US Department of Commerce, National Oceanic and Atmospheric Administration, National Weather Service, Office of Meteorology, Program and Plans Division.
Moustafa, S.E., Rennermalm, A.K., Román, M.O., Wang, Z., Schaaf, C.B., Smith, L.C., Koenig, L.S., Erb, A., 2017. Evaluation of satellite remote sensing albedo retrievals over the ablation area of the southwestern Greenland ice sheet. Remote Sens. Environ. 198, 115–125.
NASM, 2018. Thriving on Our Changing Planet: A Decadal Strategy for Earth Observation from Space. The National Academies Press, Washington, DC. http://dx.doi.org/10.17226/24938.
Nicodemus, F.E., 1977. Geometrical considerations and nomenclature for reflectance. In: National Bureau of Standards Monograph, No. 160. Washington, DC, pp. 1–52.
Nilson, T., 1971. A theoretical analysis of the frequency of gaps in plant stands. Agric. Meteorol. 8, 25–38.
NRC, 2017. A Look into Zaatari Camp during Winter | NRC [WWW Document]. World Bank URL. https://www.nrc.no/news/2016/february/a-look-into-zaatari-camp-during-winter/ (accessed 10.24.17).
Oda, Ott, L., Lauvaux, T., Feng, S., Bun, R., Roman, M., Baker, D.F., Pawson, S., 2017. Assessing Uncertainties in Gridded Emissions: A Case Study for Fossil Fuel Carbon Dioxide (FFCO2) Emission Data.
Omar, A.H., Winker, D.M., Tackett, J.L., Giles, D.M., Kar, J., Liu, Z., Vaughan, M.A., Powell, K.A., Trepte, C.R., 2013. CALIOP and AERONET aerosol optical depth comparisons: one size fits none. J. Geophys. Res. Atmos. 118, 4748–4766.
O'Sullivan, F., 2017. How Built-Out Barcelona Found Space for an Urban Forest - CityLab [WWW Document]. URL. https://www.citylab.com/solutions/2017/05/barcelona-green-urban-forest-climate-plan/526998/ (accessed 6.28.17).
Ou, J., Liu, X., Li, X., Li, M., Li, W., 2015. Evaluation of NPP-VIIRS nighttime light data for mapping global fossil fuel combustion CO_2 emissions: a comparison with DMSP-OLS nighttime light data. PLoS One 10, e0138310. http://dx.doi.org/10.1371/journal.pone.0138310.
Pahlevan, N., Sarkar, S., Devadiga, S., Wolfe, R.E., Román, M., Vermote, E., Lin, G., Xiong, X., 2017. Impact of spatial sampling on continuity of MODIS–VIIRS land surface reflectance products: a simulation approach. IEEE Trans. Geosci. Remote Sens. 55, 183–196.
Park, T., Yan, K., Chen, C., Xu, B., Knyazikhin, Y., Myneni, R., 2017. VIIRS Leaf Area Index (LAI) and Fraction of Photosynthetically Active Radiation Absorbed by Vegetation (FPAR) Product Algorithm Theoretical Basis Document (ATBD). (NASA Technical Report).
Paynter, I., Saenz, E., Genest, D., Peri, F., Erb, A., Li, Z., Wiggin, K., Muir, J., Raumonen, P., Schaaf, E.S., 2016. Observing ecosystems with lightweight, rapid-scanning terrestrial lidar scanners. Remote Sens. Ecol. Conserv. 2, 174–189.
Polivka, T.N., Wang, J., Ellison, L.T., Hyer, E.J., Ichoku, C.M., 2016. Improving nocturnal fire detection with the VIIRS day–night band. IEEE Trans. Geosci. Remote Sens. 54, 5503–5519.
Riggs, G.A., Hall, D.K., Román, M.O., 2016. NASA S-NPP VIIRS Snow Products Collection 1 User Guide 1–26. https://doi.org/10.5067/VIIRS/VNP10_L2.v001.
Riggs, G.A., Hall, D.K., Román, M.O., 2017. Overview of NASA's MODIS and VIIRS snow-cover earth system data records. Earth Syst. Sci. Data 9, 1–13. http://dx.doi.org/10.5194/essd-9-765-2017.
Roger, J.C., Vermote, E.F., Devadiga, S., Ray, J.P., 2016. Suomi-NPP VIIRS Surface Reflectance User's Guide.
Román, M., Schaaf, C.B., Yang, X., Woodcock, C.E., Strahler, A.H., Braswell, R.H., Curtis, P.S., Davis, K.J., D, D., Gu, L., Goulden, M.L., Hollinger, D.Y., Kolb, T.E., Meyers, T.P., Munger, J.W., Privette, J.L., Richardson, A.D., Wilson, T.B., Wofsy, S.C., 2009. The MODIS (Collection V005) BRDF/albedo product: assessment of spatial representativeness over forested landscapes. Remote Sens. Environ. 113, 2476–2498. http://dx.doi.org/10.1016/j.rse.2009.07.009.
Román, M.O., Gatebe, C.K., Poudyal, R., Schaaf, C.B., Wang, Z., King, M.D., 2011. Variability in surface BRDF at different spatial scales (30 m–500 m) over a mixed agricultural landscape as retrieved from airborne and satellite spectral measurements. Remote Sens. Environ. 115, 2184–2203. http://dx.doi.org/10.1016/j.rse.2011.04.012.
Román, M.O., Gatebe, C.K., Shuai, Y., Wang, Z., Gao, F., Masek, J.G., He, T., Liang, S., Schaaf, C.B., 2013. Use of in situ and airborne multiangle data to assess MODIS- and landsat-based estimates of directional reflectance and albedo. IEEE Trans. Geosci. Remote Sens. 51, 1393–1404. http://dx.doi.org/10.1109/TGRS.2013.2243457.
Román, M.O., Schaaf, C.B., Lewis, P., Gao, F., Anderson, G.P., Privette, J.L., Strahler, A.H., Woodcock, C.E., Barnsley, M., 2010. Assessing the coupling between surface albedo derived from MODIS and the fraction of diffuse skylight over spatially-characterized landscapes. Remote Sens. Environ. 114, 738–760. http://dx.doi.org/10.1016/j.rse.2009.11.014.
Román, M.O., Stokes, E.C., 2015. Holidays in lights: tracking cultural patterns in demand for energy services. Earth's Futur. 3, 182–205. http://dx.doi.org/10.1002/2014EF000285.
Ross, J., 2012. The radiation regime and architecture of plant stands, vol. 3 Springer Science & Business Media.
Roujean, J., Leroy, M., Deschanms, P., 1992. A bidirectional reflectance model of the Earth's surface for the correction of remote sensing data. J. Geophys. Res. 97, 20,420–455,468. http://dx.doi.org/10.1029/92JD01411.
Schaaf, C.B., Gao, F., Strahler, A.H., Lucht, W., Li, X., Tsang, T., Strugnell, N.C., Zhang, X., Jin, Y., Muller, J.P.J.-P., Lewis, P., Barnsley, M., Hobson, P., Disney, M., Roberts, G., Dunderdale, M., Doll, C., d'Entremont, R.P., Hu, B., Liang, S., Privette, J.L., Roy, D.P., 2002. First operational BRDF, albedo nadir reflectance products from MODIS. Remote Sens. Environ. 83, 135–148. http://dx.doi.org/10.1016/S0034-4257(02)00091-3.
Schaaf, Liu, J., Gao, F., Strahler, A.H., 2011. MODIS albedo and reflectance anisotropy products from Aqua and Terra. In: Ramachandran, B., Justice, C., Abrams, M. (Eds.), Land Remote Sensing and Global Environmental Change: NASA's Earth Observing System and the Science of ASTER and MODIS. Springer-Verlag, pp. 873 ISBN:1441967486.
Schaaf, Wang, Z., Strahler, A., 2011. Commentary on Wang and Zender—MODIS snow albedo bias at high solar zenith angles relative to theory and to in situ observations in Greenland. Remote Sens. Environ. 115, 1296–1300.
Schaepman-Strub, G., Schaepman, M.E., Painter, T.H., Dangel, S., Martonchik, J.V., 2006. Reflectance quantities in optical remote sensing-definitions and case studies. Remote Sens. Environ. 103, 27–42. http://dx.doi.org/10.1016/j.rse.2006.03.002.
Schnitt, S., Ruhtz, T., Fischer, J., Hölker, F., Kyba, C., 2013. Temperature stability of the sky quality meter. Sensors 13, 12166–12174.

Seto, K.C., Dhakal, S., 2014. Chapter 12: human settlements, infrastructure, and spatial planning. In: Clim. Chang. 2014 Mitig. Clim. Chang. Contrib. Work. Gr. III to Fifth Assess. Rep. Intergov. Panel Clim. Changpp. 67–76.

Sharma, R.C., Tateishi, R., Hara, K., Gharechelou, S., Iizuka, K., 2016. Global mapping of urban built-up areas of year 2014 by combining MODIS multispectral data with VIIRS nighttime light data. Int. J. Digit. Earth 9, 1004–1020. http://dx.doi.org/10.1080/17538947.2016.1168879.

Shi, K., Huang, C., Yu, B., Yin, B., Huang, Y., Wu, J., Chang, H., Bailang, Y., Bing, Y., Yixiu, H., Jianping, W., 2014. Evaluation of NPP-VIIRS night-time light composite data for extracting built-up urban areas. Remote Sens. Lett. 5, 358–366. http://dx.doi.org/10.1080/2150704x.2014.905728.

Shuai, Y., Schaaf, C., Zhang, X., Strahler, A., Roy, D., Morisette, J., Wang, Z., Nightingale, J., Nickeson, J., Richardson, A.D., 2013. Daily MODIS 500 m reflectance anisotropy direct broadcast (DB) products for monitoring vegetation phenology dynamics. Int. J. Remote Sens. 34, 5997–6016.

Skakun, S., Justice, C.O., Vermote, E., Roger, J.-C., 2018. Transitioning from MODIS to VIIRS: an analysis of inter-consistency of NDVI data sets for agricultural monitoring. Int. J. Remote Sens. 39, 971–992.

Strahler, A.H., Lucht, W., Schaaf, C.B., Tsang, T., Gao, F., Li, X., Muller, J.-P., Lewis, P., Barnsley, M., 1999. MODIS BRDF/Albedo Product: Algorithm Theoretical Basis Document Version 5.0. Technical Report. NASA EOS-MODIS.

Straka, W.C., Seaman, C.J., Baugh, K., Cole, K., Stevens, E., Miller, S.D., 2015. Utilization of the suomi national polar-orbiting partnership (npp) visible infrared imaging radiometer suite (viirs) day/night band for arctic ship tracking and fisheries management. Remote Sens. 7, 971–989.

Strugnell, N., Lucht, W., Schaaf, C.B., 2001. A global albedo data set derived from AVHRR data for use in climate simulations. Geophys. Res. Lett. 28, 191–194. http://dx.doi.org/10.1029/2000GL011580.

Sun, Q., Wang, Z., Li, Z., Erb, A., Schaaf, C.B., 2017. Evaluation of the global MODIS 30 arc-second spatially and temporally complete snow-free land surface albedo and reflectance anisotropy dataset. Int. J. Appl. Earth Obs. Geoinf. 58, 36–49.

Tan, B., Morisette, J.T., Wolfe, R.E., Gao, F., Ederer, G.A., Nightingale, J., Pedelty, J.A., 2008. Vegetation phenology metrics derived from temporally smoothed and gap-filled MODIS data. In: Geoscience and Remote Sensing Symposium, 2008. IGARSS 2008. IEEE International. IEEEpp. 3–593.

Tan, B., Morisette, J.T., Wolfe, R.E., Gao, F., Ederer, G.A., Nightingale, J., Pedelty, J.A., 2011. An enhanced TIMESAT algorithm for estimating vegetation phenology metrics from MODIS data. IEEE J. Sel. Top. Appl. Earth Obs. Remote Sens. 4, 361–371. http://dx.doi.org/10.1109/Jstars.2010.2075916.

Tan, B., Woodcock, C.E., Hu, J., Zhang, P., Ozdogan, M., Huang, D., Yang, W., Knyazikhin, Y., Myneni, R.B., 2006. The impact of gridding artifacts on the local spatial properties of MODIS data: implications for validation, compositing, and band-to-band registration across resolutions. Remote Sens. Environ. 105, 98–114.

Thaiutsa, B., Puangchit, L., Kjelgren, R., Arunpraparut, W., 2008. Urban green space, street tree and heritage large tree assessment in Bangkok, Thailand. Urban For. Urban Green. 7, 219–229.

Tomasi, C., Fuzzi, S., Kokhanovsky, A., 2017. Atmospheric Aerosols: Life Cycles and Effects on Air Quality and Climate. John Wiley & Sons.

UNHCR, 2017. Syria Regional Refugee Response — Emirati Jordanian Camp (Murijep al Fhoud). [WWW Document]. URL. http://data.unhcr.org/syrianrefugees/settlement.php?id=224&country=0&region=0 (accessed 10.25.17).

Vermote, E., Justice, C.O., Csiszar, I., 2014. Early evaluation of the VIIRS calibration, cloud mask and surface reflectance Earth data records. Remote Sens. Environ. 148, 134–145. http://dx.doi.org/10.1016/j.rse.2014.03.028.

Vermote, E.F., Kotchenova, S., 2008. Atmospheric correction for the monitoring of land surfaces. J. Geophys. Res. 113. http://dx.doi.org/10.1029/2007JD009662.

Walther, A., Heidinger, A.K., Miller, S., 2013. The expected performance of cloud optical and microphysical properties derived from Suomi NPP VIIRS day/night band lunar reflectance. J. Geophys. Res. Atmos. 118, 13,230–13,240. http://dx.doi.org/10.1002/2013JD020478.

Wanner, W., et al., 1997. Global retrieval of bidirectional reflectance and albedo over land from EOS MODIS and MISR data: theory and algorithm. J. Geophys. Res.-Atmos. 102 (D14), 17143–17161. http://dx.doi.org/10.1029/96JD03295.

Wang, J., Aegerter, C., Xu, X., Szykman, J.J., 2016. Potential application of VIIRS day/night band for monitoring nighttime surface PM 2.5 air quality from space. Atmos. Environ. 124, 55–63.

Wang, Z., Schaaf, C.B., Strahler, A.H., Chopping, M.J., Román, M.O., Shuai, Y., Woodcock, C.E., Hollinger, D.Y., Fitzjarrald, D.R., 2014. Evaluation of MODIS albedo product (MCD43A) over grassland, agriculture and forest surface types during dormant and snow-covered periods. Remote Sens. Environ. 140, 60–77. http://dx.doi.org/10.1016/j.rse.2013.08.025.

Wang, Z., Schaaf, C.B., Strahler, A.H., Wang, J., Woodcock, C.E., Chopping, M.J., Román, M.O., Rocha, A.V., Shuai, Y., 2012. Evaluation of moderate-resolution imaging spectroradiometer (MODIS) snow albedo product (MCD43A) over tundra. Remote Sens. Environ. 117, 264–280. http://dx.doi.org/10.1016/j.rse.2011.10.002.

Wang, Z., Schaaf, C.B., Sun, Q., Shuai, Y., Román, M.O., 2018. Capturing rapid land surface dynamics with collection V006 MODIS BRDF/NBAR/Albedo (MCD43) products. Remote Sens. Environ. 207. http://dx.doi.org/10.1016/j.rse.2018.02.001.

WMO, 2016. Observing Systems Capabilities Analysis and Review Tool: Rolling Requirements Review Process. [WWW Document]. URL. http://www.wmo.int/pages/prog/www/OSY/RRR-DB.html (accessed 8.25.17).

Wolch, J.R., Byrne, J., Newell, J.P., 2014. Urban green space, public health, and environmental justice: the challenge of making cities “just green enough.”. Landsc. Urban Plan. 125, 234–244.

Wolfe, R.E., Lin, G., Nishihama, M., Tewari, K.P., Tilton, J.C., Isaacman, A.R., 2013. Suomi NPP VIIRS prelaunch and on-orbit geometric calibration and characterization. J. Geophys. Res. Atmos. 118.

Wolfe, R.E., Nishihama, M., Fleig, A.J., Kuyper, J.A., Roy, D.P., Storey, J.C., Patt, F.S., 2002. Achieving sub-pixel geolocation accuracy in support of MODIS land science. Remote Sens. Environ. 83, 31–49.

Wolfe, R.E., Roy, D.P., Vermote, E., 1998. MODIS land data storage, gridding, and compositing methodology: level 2 grid. IEEE Trans. Geosci. Remote Sens. 36, 1324–1338.

World Bank, 2017. Rebuilding Infrastructure and Improving Access to Employment in Post Crisis Côte d'Ivoire [WWW Document]. World Bank URL. http://www.worldbank.org/en/results/2016/06/17/rebuilding-infrastructure-and-improving-access-to-employment-in-post-crisis-cote-divoire (accessed 10.24.17).

Xiao, Z., Liang, S., Wang, T., Jiang, B., 2016. Retrieval of leaf area index (LAI) and fraction of absorbed photosynthetically active radiation (FAPAR) from VIIRS time-series data. Remote Sens. 8, 351.

Xiong, X., Butler, J., Chiang, K., Efremova, B., Fulbright, J., Lei, N., McIntire, J., Oudrari, H., Sun, J., Wang, Z., 2014. VIIRS on-orbit calibration methodology and performance. J. Geophys. Res. Atmos. 119, 5065–5078.

Yang, K., Wolfe, R.E., 2001. MODIS level 2 grid with the ISIN map projection. In: Geoscience and Remote Sensing Symposium, 2001. IGARSS'01. IEEE 2001 International. IEEEpp. 3291–3293.

Yorks, J., Palm, S., McGill, M., Hlavka, D., Hart, W., Selmer, P., Nowottnick, E., 2015. CATS Algorithm Theoretical Basis Document Level 1 and Level 2 Data Products Release 1.

Yorks, J.E., McGill, M.J., Palm, S.P., Hlavka, D.L., Selmer, P.A., Nowottnick, E.P., Vaughan, M.A., Rodier, S.D., Hart, W.D., 2016. An overview of the CATS level 1 processing algorithms and data products. Geophys. Res. Lett. 43, 4632–4639. http://dx.doi.org/10.1002/2016GL068006.

Yu, B., Shi, K., Hu, Y., Huang, C., Chen, Z., Wu, J., 2015. Poverty evaluation using NPP-VIIRS nighttime light composite data at the county level in China. IEEE J. Sel. Top. Appl. Earth Obs. Remote Sens. 8, 1217–1229. http://dx.doi.org/10.1109/JSTARS.2015.2399416.

Zeng, X., Shao, X., Qiu, S., Ma, L., Gao, C., Li, C., 2018. Stability monitoring of the VIIRS day/night band over dome C with a lunar irradiance model and BRDF correction. Remote Sens. 10, 189.

Zhang, Q., Pandey, B., Seto, K.C., 2016. A robust method to generate a consistent time series from DMSP/OLS nighttime light data. IEEE Trans. Geosci. Remote Sens. 54, 5821–5831.

Zhao, F., Strahler, A.H., Schaaf, C., Yao, T., Yang, X., Wang, Z., Schull, M.A., Román, M.O., Woodcock, C.E., Olofsson, P., Ni-Meister, W., Jupp, D.L.B., Lovell, J.L., Culvenor, D.S., Newnham, G.J., 2012. Measuring gap fraction, element clumping index and LAI in Sierra forest stands using a full-waveform ground-based lidar. Remote Sens. Environ. 125, 73–79. http://dx.doi.org/10.1016/j.rse.2012.07.007.

Zhao, X., Shi, H., Yu, H., Yang, P., 2016. Inversion of nighttime PM2. 5 mass concentration in Beijing based on the VIIRS day-night band. Atmosphere (Basel). 7, 136.